MODELING OF RUPTURE PROPAGATION USING HIGH-ORDER MIMETIC FINITE DIFFERENCES

By

Otilio Rojas[1] *(rojas@sciences.sdsu.edu)*,
Steven Day[2] *(day@moho.sdsu.edu)*,
Jose Castillo[1] *(castillo@myth.sdsu.edu)* and,
Luis A. Dalguer[2] *(ldalguer@moho.sdsu.edu)*

[1]Computational Science Research Center, San Diego State University, San Diego, CA, USA.
[2]Department of Geological Sciences, San Diego State University, San Diego, CA, USA.

Submitted to:
Geophysical Journal International
May 10, 2007

Revised September 28, 2007

SUMMARY

We present a split-node finite difference (FD) method for modeling shear ruptures that is consistently fourth-order accurate in its spatial discretization, both in the interior of the model and at the fault. The method, called Mimetic Operator Split Node (MOSN), uses a staggered grid, and the fault plane is discretized using split nodes for both discontinuous displacement and discontinuous stress components. The method differs in several ways from previous FD methods for rupture modeling. (1) It uses one-sided differentiation (in the fault-normal direction) to retain high-order accuracy at the discontinuity. (2) The one-sided differentiation is implemented with mimetic FD operators that conserve the integration-by-parts formula (including boundary terms) in discrete form. (3) The mimetic operators lead naturally to the evaluation of conjugate tractions at the split-node displacement sites, as required to apply the frictional-sliding boundary conditions. In the interior of the grid, the mimetic operators reduce to the conventional fourth-order staggered-grid FD operators. We verify the accuracy of the MOSN method using two test problems: a fixed-speed rupture case (Kostrov's problem), and the case of a spontaneous rupture with slip-dependent friction. In the former test, comparisons of slip and shear stress waveforms confirm the convergence of numerical results to the analytical solution as the grid is refined. In the latter test, assessment is based on both qualitative waveform characteristics and a quantitative convergence analysis that uses error metrics in rupture time, final slip, and peak slip rate. Compared with a previously verified second-order scheme, the MOSN method shows significant reduction in artifacts attributable to numerical dispersion and also yields a considerable improvement in rupture arrival times. While from a practical standpoint the performance gains of MOSN over the second-order scheme are considerable, MOSN has comparatively poorer convergence rates, and loses its advantage in accuracy in the limit of very small spatial steps. We attribute the relatively low convergence rates to our use of a friction law that induces gradient

discontinuities in the fault traction, violating the smoothness assumptions underlying the accuracy estimates, a limitation which may not apply to more complex, experimentally-derived friction laws with smooth dependence on slip-rate and state variables. Our current implementation is two dimensional and assumes a straight fault, but the method is extensible to more general 3D geometries.

INTRODUCTION

The dynamics of a shear crack confined in a linearly elastic continuum has been actively researched because of its potential contributions to understanding earthquake physics and ground motion excitation. Solutions are typically given in terms of the slip between the walls of the fault and evolving stress fields as the rupture progresses. Analytical results are available for a few geometrically simple cases with prescribed rupture velocity (e.g., Kostrov, 1964; Burridge & Willis, 1969; Richards, 1973; Richards, 1976). More realistic models allow spontaneous rupture propagation over a fault surface where frictional sliding is controlled by a constitutive law. Given the initial stress distribution, elastic properties of the continuum, and geometry of the fault, the friction law governs the evolution and arrest of a spontaneous rupture. This friction law may depend on slip, slip rate, effective normal traction, and various state variables (Dieterich, 1979; Ruina, 1983). Some friction laws admit stationary contact, in which case the shear traction is bounded by the maximum frictional strength of the fault given by the constitutive relation, and no slip is permitted where shear traction is less than the frictional strength. In that case, spontaneous rupture represents a non-linear and mixed boundary problem, where respective domains of dynamic and kinematic boundary conditions are time dependent and not known a priori. In general, analytical solutions are not available, and we depend upon numerical solvers that model the elastic motion in the interior coupled to frictional sliding along the fault plane.

The problem is computationally intensive, and precise and flexible numerical techniques are still a subject of research.

Accuracy of numerical modeling of rupture dynamics is highly dependent on the implementation of the faulting boundary conditions. The traction-at-split-node (TSN) method was developed by Andrews (1973, 1976a, 1976b), and extended to 3D by Day (1977, 1982). It has proven to be a precise and efficient implementation of these conditions in the framework of finite-differences (FD) (e.g., Andrews, 1999; Dalguer & Day, 2006) and finite-elements (e.g., Oglesby *et al*., 1998; Aagaard et al., 2001). Our development here parallels that of Day et al. (2005) (hereafter D05) and Dalguer & Day (2007) (hereafter DD07).

The TSN method represents a fault as a surface discretized by a set of double nodes called split nodes. Each half of a split node belongs to only one side of the fault, and it may experience motion relative to its counterpart. Thus, velocity and displacement discontinuities (slip and slip rate) across the fault are allowed. Elastic deformations at each side of the fault are accounted by a separate application of equations of motion at each half of the split node, and the continuity in surface traction (frictional resistance and normal traction) controls the interaction between the two halves of the split node (Andrews, 1999; D05; Moczo, *et al.*, 2006). FD implementations of the TSN technique have used two types of grids, the partially staggered grid (PSG), and the standard staggered grid (SSG). A recent review of these grids was done by Moczo *et al.* (2006) (where a SSG is just referred to as a staggered grid). In a PSG, all components of particle velocity are defined at the same grid point, while the whole stress tensor is placed in the cell centers. In this case, the fault coincides with a plane of split velocity nodes, e.g., the DFM algorithm of Day (1982). On the other hand, the SSG defines different grid points to accommodate each particle velocity component (with corresponding displacement), and the

shear stress components are also distributed around the unit cell. This grid has been widely used in 2D and 3D seismic wave propagation (Madariaga, 1976; Virieux, 1986; Levander, 1988; Graves, 1996; Pitarka, 1999; Kristek, *et al.*, 2002; Olsen, *et al.*, 2006). Recently, DD07 introduced an implementation of the TSN method on a velocity-stress SSG, where split nodes are used to represent both the velocity and stress components that are discontinuous across the fault. They compared this method, referred as SGSN (Staggered Grid Split Node), with DFM by solving a benchmark problem due to Harris et al. (2004), measuring accuracy in terms of three error metrics: rupture arrival times, final slip, and slip rate. This study revealed similar order of convergence of these two algorithms as the grid interval decreases. In consequence, DD07 concluded that the grid geometry (i.e., PSG versus SSG) has minimal influence on the accuracy of the TSN implementation, compared with the large influence of different fault-boundary formulations found by Dalguer & Day (2006).

A common aspect of the SGSN and DFM algorithms is that both use second-order spatial discretization of the boundary conditions at the split nodes. DFM is second-order everywhere, while in the case of SGSN, fourth-order spatial differencing is used in most of the continuum, but reduced to second order at points near the fault. Other FD versions of the TSN technique are also limited to second order accuracy, e.g., the original scheme introduced by Andrews (1973; 1999).

In this work, we develop a split-node FD method for modeling shear ruptures that is consistently fourth-order accurate in its spatial discretization. That is, it maintains fourth-order accuracy both in the interior of the model and at the fault. This consistency in order of accuracy at boundaries is achieved very naturally in higher-order variational methods such as the Spectral Element Method (e.g., Ampuero, 2002; Madariaga et al, 2006; Festa and Villote, 2006), but

requires special boundary treatment in FD. Specifically, the use of one-sided stencils at split nodes allows a fourth-order accurate discretization of the jump conditions without requiring the differencing stencil to cross physical discontinuities at the fault. The same order of accuracy is maintained in the interior discretization of the elastodynamic wave equations (which are written in a displacement-stress form). We focus here on comparing the accuracy of the second- and fourth-order schemes, and therefore limit the implementation to 2D, in-plane motion.

The method presented here for spontaneous rupture problems, based on one-sided, fourth-order stencils, was first introduced in Rojas *et al.* (2006) and further described in Rojas et al. (2007). Prior to this, Kristek et al. (2002) introduced a fully fourth-order method for seismic wave propagation problems based on one-sided stencils for the free-surface boundary of the halfspace, and that approach was subsequently extended to the spontaneous rupture problem by Kristek et al. (2006), and Moczo et al. (2007). The main difference between our method and that of the latter authors is in the method of construction of the one-sided operators. In the current work, with an eye toward future developments, we use the mimetic operators introduced by Castillo *et al.* (2001) and Castillo & Grone (2003). Mimetic operators are so called because, by construction, they mimic certain integral identities obeyed by their continuous counterparts. In this case, the operators obey a summation-by-parts formula that is the discrete analogue of the Green-Stokes theorem. We will call this family of differentiators *Castillo-Grone* operators, and we call the resulting rupture simulation method MOSN (Mimetic Operators and Split Nodes).

While MOSN only uses mimetic operators in a 1D sense, i.e., to handle differentiation in the fault-normal direction, the approach can be extended to yield fully mimetic solutions to rupture problems in 2D and 3D (Ely et al., 2006), which in turn translates into important properties of those solutions, including reciprocity and energy conservation. The formulation in terms of these operators also has at least two further advantages: (i) the coincident location of

traction components at split displacement (and velocity) nodes (and conversely, of displacement/velocity components at split stress nodes in the method of DD07), which is a requirement of the TSN method, is already inherent in the theory of the mimetic discretization of the fault-normal derivatives, and does not require an auxiliary construction for its implementation; and (ii) the methodology of Castillo et all. (2001) already provides sixth-order accurate counterparts for the fourth-order operators used here. Mimetic discretization has been successfully applied to diffusion problems (Shaskov & Steinberg, 1996; Hyman *et al.* 1997; Hyman *et al.* 2002), Maxwell equations (Hymann & Shaskov, 1999), and recently in seismic wave propagation (Strand, 1999; Ely *et al.*, 2007).

The assessment of the MOSN method is performed by solving two test cases. First, we solve numerically the self-similar propagation of a Mode II shear crack (Kostrov's problem), for which an analytic solution is known. Next, we present results for a spontaneous rupture problem that is a 2D (in-plane motion) analog of Version 3 SCEC 3D benchmark problem due to Harris *et al.* (2004). We use the DFM algorithm to generate a reference solution and then study accuracy and convergence of MOSN solutions following the methodology used in D05 and DD07. For relatively coarse grids, rupture arrival times are better modeled by the MOSN method than by the (second-order) DFM algorithm, as are the time histories of shear stress and slip velocity. The apparent convergence rate of MOSN is lower than that of DFM, however, and its advantage in accuracy disappears for sufficiently small spatial step size. The low apparent convergence rate may be a result of discontinuous derivatives in the stress and velocity fields due to lack of smoothness of the assumed friction law. Nonetheless, for accuracy levels of practical interest (i.e., ~1% in rupture time), the MOSN method produces large gains in computational efficiency, and may prove even more advantageous for applications to inherently smooth friction laws such as rate- and state-dependent laws (e.g., Dieterich, 1979; Ruina, 1983).

Here we present only the implementation for a fault coincident with a Cartesian coordinate plane. We also focus specifically on discretization of the fault surface, which we therefore embed in an unbounded space. While the presentation here is 2D, the MOSN method can be immediately generalized to 3D staggered grids by using the technique of DD07 to align the slip and frictional-stress vectors.

PROBLEM STATEMENT: IN-PLANE SHEAR RUPTURES

In this section, we present the mathematical formulation of the 2D in-plane rupture propagation problems that are the subject of our numerical studies. We consider an infinite, isotropic, and linearly elastic volume embedding a planar surface Σ across which there may be a time-dependent discontinuity in the displacement. In applications to earthquakes, the surface Σ represents a fault, the discontinuity is the fault slip, and the initiation of unstable slip is referred to as rupture. We take Σ to be the plane $z = 0$, and consider a shear rupture in which the displacement is independent of the y coordinate and has only x and z components (so slip is in the x direction). Elastic disturbances caused by the rupture satisfy the equations of motion,

$$\rho \ddot{u}_x = \tau_{xx,x} + \tau_{xz,z} \tag{1.1}$$

$$\rho \ddot{u}_z = \tau_{xz,x} + \tau_{zz,z} \tag{1.2}$$

and the Hooke's law,

$$\begin{aligned} \tau_{xx} &= (\lambda + 2\mu) u_{x,x} + \lambda u_{z,z} \\ \tau_{zz} &= (\lambda + 2\mu) u_{z,z} + \lambda u_{x,x} \\ \tau_{xz} &= \mu \left(u_{x,z} + u_{z,x} \right) \end{aligned} \tag{2}$$

Here, we adopt the notation $\ddot{u}_x = \partial^2 (u_x) / \partial t^2$, $u_{x,x} = \partial(u_x)/\partial x$, $\tau_{xx,x} = \partial \tau_{xx} / \partial x$, and so on.

Parameters in this model are the density ρ and Lame constants λ and μ. Dependent variables are the components of the displacement vector $\mathbf{u} = (u_x, u_z)$, and the components of the incremental

stress tensor are τ_{xx}, τ_{zz}, and τ_{xz}, measured with respect to an initial distribution (in static equilibrium) given by τ_{xx}^0, τ_{zz}^0 and τ_{xz}^0. Additional parameters are the *P*- and *S*-wave speeds, denoted as α and β, respectively, corresponding to $\alpha = \sqrt{(\lambda + 2\mu)/\rho}$ and $\beta = \sqrt{\mu/\rho}$.

Solution of (1.1) and (1.2) requires an appropriate set of initial and boundary conditions. Assuming quiescence prior to rupture initiation at $t = 0$, we have that $\mathbf{u} = \dot{\mathbf{u}} = \mathbf{0}$ everywhere for $t \leq 0$. Fault boundary conditions at $z = 0$ only allow in-plane motion, preclude both opening of the fault and interpenetration of the fault materials, and require continuity of normal and shear traction at the fault. Thus, u_z, τ_{zz}, and τ_{xz} are continuous at $z = 0$. On the other hand, the horizontal particle displacement u_x may have a discontinuity across the axis x and this jump is called slip s. Let us designate the limiting values for u_x at this interface as,

$$u_x^{\pm}(x, z = 0, t) = \lim_{\varepsilon \to 0} u_x(x, z = \pm\varepsilon, t),\ \varepsilon > 0,$$

Where the superscripts (+) and (-) denote, respectively, the plus-side and minus-side part of the fault plane. Thus, $s = u_x^+ - u_x^-$. The time derivative of the slip, $\dot{s}$ is known as the slip rate or slip velocity. In this work, we solve numerically two different in-plane problems which demand distinct mathematical statements for their boundary conditions. Particular expressions are given below for each case.

A self-similar case

In addition to the conditions proposed above, let us assume that the medium is homogenous and $\tau_{xx}^0 = \tau_{zz}^0 = 0$, while τ_{xz}^0 is constant. The dynamics of a self-similar crack with a bilateral propagation at a constant velocity v_R lower than the Rayleigh velocity can be described analytically using the solution due to Kostrov (1964). As the rupture evolves, the total shear

traction vanishes on the crack surface, while no slip is experienced elsewhere. The solution of this problem satisfies the symmetry (or antisymmetry) properties of a mode II crack problem with respect to $z = 0$ (e.g., see Broberg, 1999). Specifically, u_z, and τ_{xz} are even functions of z, while u_x, τ_{xx} *and* τ_{zz} are odd functions. Taking the symmetry into account, we solve (1) and (2) in z > 0, with linear, mixed boundary conditions

$$\begin{cases} \tau_{xz} = -\tau_{xz}^0 & \text{for } z = 0, \quad |x| \le v_R\, t \\ u_x = 0 & \text{for } z = 0, \quad |x| > v_R\, t. \\ \tau_{zz} = 0 & \text{for } z = 0 \end{cases} \tag{3}$$

Results from the application of our numerical scheme to this problem are given in a section below. Expressions for the analytical solution can be found in the original paper by Kostrov (1964) and in later references (e.g., Richards, 1973).

Spontaneous rupture

Nonlinearity is introduced in our rupture model by allowing the rupture velocity to be implicitly controlled by the frictional behavior relating traction to slip at the fault surface. We formulate the jump conditions at $z = 0$ as in D05, in terms of the total shear traction $T = \tau_{xz} + \tau_{xz}^0$, in the form

$$|T| \le \tau_c \tag{4}$$

$$\tau_c\, \dot{s} - T|\dot{s}| = 0. \tag{5}$$

Equation (4) implies that T is bounded above by the frictional strength of the fault τ_c. On the other hand, equation (5) allows a nonzero velocity discontinuity just when the magnitude of the total shear traction reaches τ_c. In general, τ_c evolves according to a constitutive law which may depend upon the total normal stress, slip, slip velocity and other mechanical, thermal, and state variables (e. g., Bizarri *et al.*, 2001).

In this work, we adopt the slip-weakening (SW) model introduced by Ida (1972) and Palmer and Rice (1973) as the friction law. The frictional strength τ_c is assumed to be a fraction of the total normal stress $\sigma_n = \tau_{zz} + \tau_{zz}^0$ (taken negative in compression)

$$\tau_c = -\sigma_n \mu_f(l) \ . \tag{6}$$

The coefficient of friction $\mu_f(l)$ depends on the slip path length l, defined as $\int_0^t \dot{s}(t')dt'$, through the slip-weakening relationship,

$$\mu_f(l) = \begin{cases} \mu_s - (\mu_s - \mu_d)l/d_0 & l < d_0 \\ \mu_d & l \geq d_0 \end{cases} \tag{7}$$

Parameters μ_s and μ_d are the coefficients of static and dynamic friction, respectively, and d_0 is the critical slip-weakening distance. This SW model ignores the effect of parameters such as slip rate, pore fluids, and temperature, among others that are likely to be important in frictional sliding under the conditions of natural earthquakes (e.g., Rice, 2006). However, it has been widely used in rupture dynamics and earthquake simulation (e.g., Andrews, 1976a; Andrews, 1976b; Andrews,1999; Madariaga *et al.*, 1998; Harris *et al.*, 2004; D05; Olsen *et al.*, 2006; DD07), and the SW model therefore provides a convenient standard for comparison with previous numerical solution methods.

NUMERICAL SCHEME

The simple planar geometry of the shear crack problems addressed in this work allows the implementation of our numerical method on a rectangular SSG. We further restrict the development here to 2D, although it generalizes immediately to 3D. Apart from the fault plane, this grid is similar to the one originally used by Madariaga (1976) and later by Virieux & Madariaga (1982) in the solution of two dimensional crack problems. Numerical differentiation with respect to each spatial coordinate is performed by using an appropriate staggered FD stencil

along each gridline. For a consistent fourth-order discretization of both elastodynamic equations and jump conditions, we require one-sided stencils for differentiation along gridlines orthogonal to the fault in a neighborhood of this boundary, while centered stencils can be used elsewhere. To facilitate the implementation of the TSN method (detailed below), we follow Dalguer & Day (DD07) by (i) introducing split nodes to represent the discontinuities that are present in both stress and velocity components located on the fault-plane, and (ii) locating certain stress and velocity components together at the split nodes. The Dalguer and Day method differs from earlier split node methods in its explicit representation of stress-component discontinuities (in addition to the conventional velocity discontinuities), and by its coincident location of fault-normal velocity at split-stress nodes (complementary to the conventional device of locating fault shear stress at split-velocity nodes). This method requires FD formulas capable of differentiating both velocity (or displacement) and stress fields throughout the grid, explicitly taking into account both the fault plane discontinuities and the coincident location of stress and velocity components at the split nodes. We construct such formulas by combining one-sided difference operators from the Castillo-Grone family of mimetic operators. Below, we describe this construction process, and then we detail the application of the resulting difference operators in our TSN implementation.

Mimetic finite differences

We consider two functions $f(z)$ and $v(z)$ on the interval [a,b], $a < 0 < b$, both of which are smooth, apart from a possible discontinuity of v at $z = 0$. We want to construct approximations for dv/dz and df/dz, respectively, that (i) are everywhere fourth-order accurate, and (ii) satisfy a discrete analog of the integration by parts formulas on each of the two halflines terminating at the discontinuity,

$$\int_a^{0^-} \frac{dv}{dz} f dz = v(0^-) f(0) - v(a) f(a) - \int_a^{0^-} v \frac{df}{dz} dz$$
$$\int_{0^+}^b \frac{dv}{dz} f dz = -v(0^+) f(0) + v(b) f(b) - \int_{0^+}^b v \frac{df}{dz} dz \quad . \tag{8}$$

We refer to the second as the conservation criterion (for example, in the case where v is velocity and f is stress, it is a statement of discrete energy conservation in 1D). Evaluations of v and f are placed on a staggered grid, with equal-sized cells $\left[z_j, z_{j+1}\right]$, $j = -M, \ldots -2, -1, 0, 1, 2, \ldots N$, with $z_j = jh$, $a = -Mh$, $b = Nh$. Points z_j are called nodes, and z_0 is a split node. In addition, the cell centers are indexed with half-integer indices, $z_{j+1/2} = \left(z_j + z_{j+1}\right)/2$. We define vector $\mathbf{v}$ in terms of values of v at the nodes (including the split node) and $\mathbf{f}$ in terms of values of f at the cell centers as well as at the split node,

$$\mathbf{v} = \begin{bmatrix} \mathbf{v}^- \\ \mathbf{v}^+ \end{bmatrix}, \tag{9}$$

where

$$\begin{aligned} \mathbf{v}^- &= \left(v(z_{-M}), \ldots v(z_{-2}), v(z_{-1}), v^-\right)^T \\ \mathbf{v}^+ &= \left(v^+, v(z_1), v(z_2), \ldots, v(z_N)\right)^T \\ v^\pm &= v\left(0^\pm\right) \end{aligned} \quad , \tag{10}$$

and

$$\mathbf{f} = \begin{bmatrix} \mathbf{f}^- \\ \mathbf{f}^+ \end{bmatrix}, \tag{11}$$

where

$$\begin{aligned} \mathbf{f}^- &= \left(f(z_{-M}), f\left(z_{-M+1/2}\right), \ldots f\left(z_{-3/2}\right), f\left(z_{-1/2}\right), f_0\right)^T \\ \mathbf{f}^+ &= \left(f_0, f\left(z_{1/2}\right), f\left(z_{3/2}\right), \ldots . f\left(z_{N-1/2}\right), f\left(z_N\right)\right)^T \\ f_0 &= f\left(0^+\right) = f\left(0^-\right) \end{aligned} \quad , \tag{12}$$

(thus, **v** has dimension M+N+2, and **f** has dimension M+N+4). Fig. 1 shows the staggered distribution of the vector components. The approximations to dv/dz and df/dz are, respectively, **Dv** and **Gf**, where **D** is an (N+M) x (N+M+2) matrix and **G** is an (N+M+2) x (N+M+4) matrix. As indicated by Fig. 1, the derivative approximation D**v** maps **v** from nodes (including the split node) to cell centers, and **Gf** maps **f** from cell centers (plus endpoints and split node) to nodes (including the split node).

We can construct operators **D** and **G** by combining two separate one-sided difference operators, applied to $\mathbf{v}^+$ and $\mathbf{v}^-$, respectively (and likewise to $\mathbf{f}^\pm$). If we do so using the fourth-order difference operators developed by Castillo et al. (2001) and Castillo and Grone (2003), the resulting **D** and **G** will meet our stipulated order-of-accuracy and conservation criteria. Those authors describe a three-parameter family of operators that satisfy those criteria when applied to smooth functions on a finite interval. We choose their parameters, which they call (α, β, γ), equal to $(0, 0, -1/24)$, since this choice minimizes the bandwidth of the operators. We designate the resulting Castillo-Grone operators, for an interval of length *Kh*, by $\mathrm{D}_{CG}^{(K)}$ (a K by K+1 matrix) and $\mathrm{G}_{CG}^{(K)}$ (a K+1 by K+2 matrix), for which the explicit expressions are

$$\mathrm{D}_{CG}^{(K)} = \begin{bmatrix} -\frac{1045}{1142} & \frac{909}{1298} & \frac{201}{514} & -\frac{1165}{5192} & \frac{129}{2596} & -\frac{25}{15576} & 0 & \cdots \\ \frac{1}{24} & -\frac{27}{24} & \frac{27}{24} & -\frac{1}{24} & 0 & 0 & 0 & \cdots \\ 0 & \frac{1}{24} & -\frac{27}{24} & \frac{27}{24} & -\frac{1}{24} & 0 & 0 & \cdots \\ 0 & 0 & \frac{1}{24} & -\frac{27}{24} & \frac{27}{24} & -\frac{1}{24} & 0 & \cdots \\ \vdots & \vdots & \vdots & \vdots & \vdots & \vdots & \vdots & \cdots \end{bmatrix}, \qquad (13)$$

$$\mathrm{G}_{CG}^{(K)} = \begin{bmatrix} -\frac{1775}{528} & \frac{1790}{407} & -\frac{2107}{1415} & \frac{1496}{2707} & -\frac{272}{2655} & \frac{25}{9768} & 0 & \cdots \\ \frac{16}{105} & -\frac{31}{24} & \frac{29}{24} & -\frac{3}{40} & \frac{1}{168} & 0 & 0 & \cdots \\ 0 & \frac{1}{24} & -\frac{27}{24} & \frac{27}{24} & -\frac{1}{24} & 0 & 0 & \cdots \\ 0 & 0 & \frac{1}{24} & -\frac{27}{24} & \frac{27}{24} & -\frac{1}{24} & 0 & \cdots \\ \vdots & \vdots & \vdots & \vdots & \vdots & \vdots & \vdots & \cdots \end{bmatrix}. \tag{14}$$

In each case, the lower half, not shown, is determined by a centro-skew-symmetric condition, i.e., the components of d_{ij} and g_{ij} of $\mathrm{D}_{CG}^{(K)}$ and $\mathrm{G}_{CG}^{(K)}$, respectively, have skew symmetry under combined column reversal plus row reversal:

$$\begin{aligned} d_{ij} &= -d_{K-i,K+1-j} \\ g_{ij} &= -g_{K+1-i,K+2-j} \end{aligned}. \tag{15}$$

$\mathrm{D}_{CG}^{(N)}$ and $\mathrm{G}_{CG}^{(N)}$ applied to $\mathbf{v}^+$ and $\mathbf{f}^+$ satisfy the order-of-accuracy and conservation criteria on $[z_0, z_N]$, and likewise $\mathrm{D}_{CG}^{(M)}$ and $\mathrm{G}_{CG}^{(M)}$ applied to $\mathbf{v}^-$ and $\mathbf{f}^-$ satisfy the order-of-accuracy and conservation criteria on $[z_{-M}, z_0]$. Thus, the matrix operators defined by

$$\begin{aligned} \mathrm{D} &= \begin{bmatrix} \mathrm{D}_{CG}^{(M)} & 0 \\ 0 & \mathrm{D}_{CG}^{(N)} \end{bmatrix}, \\ \mathrm{G} &= \begin{bmatrix} \mathrm{G}_{CG}^{(M)} & 0 \\ 0 & \mathrm{G}_{CG}^{(N)} \end{bmatrix}, \end{aligned} \tag{16}$$

applied to (discontinuous) $\mathbf{v}$ and $\mathbf{f}$, satisfy the conservation and order-of-accuracy criteria on the full interval $[z_{-M}, z_N]$. To emphasize the centro-skew-symmetry, we write out explicitly the portion of $\mathbf{D}$ centered on the discontinuity,

$$
\mathrm{D} = \begin{bmatrix}
 & \vdots & \vdots & \vdots & \vdots & \vdots & \vdots & \vdots & \vdots & \vdots & \vdots & \vdots & \vdots & \vdots & \vdots & \vdots & \\
\cdots & 0 & 0 & \frac{1}{24} & -\frac{27}{24} & \frac{27}{24} & -\frac{1}{24} & 0 & 0 & 0 & 0 & 0 & 0 & 0 & 0 & \cdots \\
\cdots & 0 & 0 & 0 & \frac{1}{24} & -\frac{27}{24} & \frac{27}{24} & -\frac{1}{24} & 0 & 0 & 0 & 0 & 0 & 0 & 0 & \cdots \\
\cdots & 0 & \frac{25}{15576} & -\frac{129}{2596} & \frac{1165}{5192} & -\frac{201}{514} & -\frac{909}{1298} & \frac{1045}{1142} & 0 & 0 & 0 & 0 & 0 & 0 & 0 & \cdots \\
\cdots & 0 & 0 & 0 & 0 & 0 & 0 & 0 & -\frac{1045}{1142} & \frac{909}{1298} & \frac{201}{514} & -\frac{1165}{5192} & \frac{129}{2596} & -\frac{25}{15576} & 0 & \cdots \\
\cdots & 0 & 0 & 0 & 0 & 0 & 0 & 0 & \frac{1}{24} & -\frac{27}{24} & \frac{27}{24} & -\frac{1}{24} & 0 & 0 & 0 & \cdots \\
\cdots & 0 & 0 & 0 & 0 & 0 & 0 & 0 & 0 & \frac{1}{24} & -\frac{27}{24} & \frac{27}{24} & -\frac{1}{24} & 0 & 0 & \cdots \\
 & \vdots & \vdots & \vdots & \vdots & \vdots & \vdots & \vdots & \vdots & \vdots & \vdots & \vdots & \vdots & \vdots & \vdots &
\end{bmatrix}. \qquad (17)
$$

Note that, away from the discontinuity, both mimetic operators **D** and **G** reduce to the standard staggered, centered, fourth-order difference operator (e.g., Levander, 1988) with weights $(-1/24, 27/24, -27/24, 1/24)$.

In the following section, we will make explicit use of the stencils comprised in **G** and **D**. We will refer to each coefficient by its location in the $\mathrm{D}_{CG}^{(K)}$ and $\mathrm{G}_{CG}^{(K)}$ matrices, thus $-1775/528$ corresponds to g_{11}, and so on.

Mimetic Operators and Split Nodes (MOSN)

This section focuses on the application of operators **G** and **D** in the discretizaton of the elastodynamic system (1) - (2), and the new TSN implementation of the faulting boundary conditions. Fig. 2 depicts the 2D SSG used in the spatial discretization of the medium, material properties and elastic fields. Only the part of the grid on the positive side of the fault is shown. Indices for grid points at which displacement component u_x are located are integer pairs (i,j), while indices for u_z and the 3 stress components are offset from (i,j) by $\pm 1/2$ in one or two directions. Density is defined at the same locations as u_x, while Lame constants are defined at grid points that coincide with normal stresses. Thus, discrete values of material properties are indexed as $\rho_{i,j}$, $\lambda_{i+1/2,j}$, and $\mu_{i+1/2,j}$ relative to the grid point (i,j). We use averaging to interpolate material properties at the grid points where they are required. In the case of an interior node, that

is, for (*i,j*) not on the fault plane, the averaging formulas proposed by Graves (1996) (arithmetic for density and harmonic for Lame constants) are used to approximate density at the grid point (*i+1/2,j+1/2*) and shear modulus at the node (*i,j+1/2*), i.e.,

$$\begin{aligned} \bar{\rho}_{i+1/2,j+1/2} &= \frac{1}{4}\left(\rho_{i,j} + \rho_{i,j+1} + \rho_{i+1,j} + \rho_{i+1,j+1}\right), \\ \bar{\mu}_{i,j+1/2} &= 4\left(\mu_{i-1/2,j}^{-1} + \mu_{i+1/2,j}^{-1} + \mu_{i-1/2,j+1}^{-1} + \mu_{i+1/2,j+1}^{-1}\right)^{-1} \end{aligned} . \tag{18}$$

These expressions have to be modified for nodal values on the fault plane, as noted below.

We approximate all the derivatives with respect to *x* required by (1) and (2) using the usual staggered, centered fourth-order difference stencil $(-1/24, 27/24, -27/24, 1/24)$ (e.g., Levander, 1988). To accommodate the discontinuity at the fault plane, the *z* derivatives in equations (1) and (2) are instead approximated by the difference operators **D** and **G** given in (16), in the manner detailed later in this section. However, as we have already noted, away from the fault the latter operators also reduce to the standard stencil. Thus, apart from the immediate vicinity of the fault, our method is identical to the usual fourth-order FD method.

We take the fault plane to be at *z = 0,* with index j_0 (note that we set $j_0 = 0$ in describing the mimetic differentiators in the previous section). At the fault plane nodes, both the material properties (ρ, λ, μ) and the discontinuous field variables (u_x, τ_{xx}) are assigned separately to the two parts of the split nodes, with the two parts denoted $\rho_i^{\pm}$, $\lambda_{i+1/2}^{\pm}$, $\mu_{i+1/2}^{\pm}$, $\left(u_x^{\pm}\right)_i$, and $\left(\tau_{xx}^{\pm}\right)_{i+1/2}$. Since all split variables are indicated by the presence of plus or minus superscripts, and all are located on the fault plane, the *j* index is redundant, and we suppress it for the split variables. We follow DD07 and apply a one-sided averaging approach to interpolate density at the *i+1/2* split node and shear modulus at the *i* split node, i.e.,

$$\bar{\rho}^{\pm}_{i+1/2} = \frac{1}{2}\left(\rho^{\pm}_{i} + \rho^{\pm}_{i+1}\right), \qquad \bar{\mu}^{\pm}_{i} = 2\left[\left(\mu^{\pm}_{i-1/2}\right)^{-1} + \left(\mu^{\pm}_{i+1/2}\right)^{-1}\right]^{-1} \quad . \tag{19}$$

Dalguer et al. (2006) have shown that this material-properties averaging scheme performs well on, for example, the very challenging problem of rupture on an interface separating materials of contrasting elastic properties. When *x* derivatives of split quantities are required, we form a separate plus- and minus-side derivatives, using the plus- and minus-indexed quantities, respectively, still with the standard fourth-order stencil (since there is no discontinuity crossed in the *x* direction, even though the derivative itself is discontinuous in the *z* direction).

To apply **D** and **G** to *z* differentiation at and near the fault, we introduce a special arrangement of discrete fields at the fault. This arrangement brings our problem into correspondence with the arrangement of function evaluations in vectors **v** and **f** (Equations 9-12) used for the construction of **D** and **G** in the previous section.

First, we consider lines of constant (integer) values of the *x* index *i*, that is, lines parallel to the *z* axis and containing the split $u_x^{\pm}$ sites. At each of those split node sites (semi-circles in Fig. 2), we locate an extra evaluation of the continuous stress component τ_{xz}, denoted by $\left(\tau^{*}_{xz}\right)_i$. This extra function evaluation is required to conform to the mimetic formulation, i.e., for fixed *i*, $\left(u_x\right)_{ij}$ (augmented by $\left(u_x^{\pm}\right)_i$) takes the role of **v** ($\left(u_x^{\pm}\right)_i$ taking the role of $v^{\pm}$), and $\left(\tau_{xz}\right)_{i,j+1/2}$ (augmented by $\left(\tau^{*}_{xz}\right)_i$) takes the role of **f** ($\left(\tau^{*}_{xz}\right)_i$ taking the role of f_0). Summarizing this correspondence for constant integer *i,* we have:

v corresponds to $\left(\ldots,\left(u_x\right)_{i,j_0-2},\left(u_x\right)_{i,j_0-1},\left(u_x^{-}\right)_i,\left(u_x^{+}\right)_i,\left(u_x\right)_{i,j_0+1},\left(u_x\right)_{i,j_0+2},\ldots\right)^T$

f corresponds to $\left(\ldots,\left(\tau_{xz}\right)_{i,j_0-3/2},\left(\tau_{xz}\right)_{i,j_0-1/2},\left(\tau^{*}_{xz}\right)_i,\left(\tau^{*}_{xz}\right)_i,\left(\tau_{xz}\right)_{i,j_0+1/2},\left(\tau_{xz}\right)_{i,j_0+3/2},\ldots\right)^T$

Then, z differentiation at fixed integer i is performed using operator **D** to differentiate u_x and operator **G** to differentiate τ_{xz}.

Second, we consider line of constant half-integer values $i+1/2$ of the x index, containing the split $\tau_{xx}^{\pm}$ sites. No z differentiation of τ_{xx} is required in this problem, and the other fields present are continuous, so we could have used ordinary two-sided differentiation along these lines. However, a natural generalization of our problem would be to allow a discontinuity in the normal displacement u_z on the fault, that is, allow fault opening (see, e.g., the formulation of D05). To allow for this generalization in the future, we use the mimetic differentiators on the $i+1/2$ lines as well. Analogously to the previous case, we locate an extra evaluation of the displacement u_z, denoted by $\left(u_z^*\right)_{i+1/2}$, at the split $\tau_{xx}^{\pm}$ site (triangles in Fig. 2). This time, for fixed $i+1/2$, $\left(\tau_{zz}\right)_{i+1/2,j}$ (including the fault-plane value $\left(\tau_{zz}\right)_{i+1/2,j_0}$) takes the role of **v** (with $\left(\tau_{zz}\right)_{i+1/2,j_0}$ taking the roles of $v^- = v^+$), and $\left(u_z\right)_{i+1/2,j+1/2}$ (augmented by $\left(u_z^*\right)_{i+1/2}$) takes the role of **f** (with $\left(u_z^*\right)_{i+1/2}$ taking the role of f_0) and in the generalization to discontinuous u_z, we would have split values $u_z^{\pm}$, and f_0 would be replaced in the mimetic formulation by unequal values $f^{\pm} = \left(u_z^{\pm}\right)_{i+1/2}$). Summarizing the correspondence for constant half-integer $i+1/2$, we have:

v corresponds to $\left(\ldots,\left(\tau_{zz}\right)_{i+1/2,j_0-2},\left(\tau_{zz}\right)_{i+1/2,j_0-1},\left(\tau_{zz}\right)_{i+1/2,j_0},\left(\tau_{zz}\right)_{i+1/2,j_0}\right.$, $\left.\left(\tau_{zz}\right)_{i+1/2,j_0+1},\left(\tau_{zz}\right)_{i+1/2,j_0+2},\ldots\right)^T$

f corresponds to $\left(\ldots,\left(u_z\right)_{i+1/2,j_0-3/2},\left(u_z\right)_{i+1/2,j_0-1/2},\left(u_z^*\right)_{i+1/2},\left(u_z^*\right)_{i+1/2},\left(u_z\right)_{i+1/2,j_0+1/2},\left(u_z\right)_{i+1/2,j_0+3/2},\ldots\right)^T$

Then, z differentiation at fixed half-integer index $i+1/2$ is performed using operator **D** to differentiate τ_{zz} and operator **G** to differentiate u_z.

Once we have approximated all spatial derivatives present in system (1)-(2), displacement fields are stepped in time at every interior grid point ($j \neq j_0$), by an explicit and second-order discretization of the time derivatives present in (1).

Next, we explain the numerical treatment of faulting boundary conditions. The application of the TSN method at a particular $u_x^{\pm}$ split node (integer index *i*), comprises two steps (Andrews, 1999): *(i)* find a total trial shear traction $\tilde{T}_i$ that gives no slip velocity (continuity of $\dot{u}_x$), and *(ii)* correct this value to the actual total shear traction T_i using a constitutive law that models the progress of the rupture and subsequent resistance to sliding. This algorithm is well suited for the case of a spontaneous rupture, where step *(i)* uses the discrete version of equation of motion (1.1) to predict $\tilde{T}_i$, followed by the correction step *(ii)* that imposes boundary conditions (4) and (5) and the friction model (6) and (7). On the other hand, in the case of the self-similar problem stated above (equations (1)–(3)), condition (3) yields the exact total shear traction T_i =0, which reduces the TSN treatment just to step *(ii)*.

We describe the implementation of steps *(i)* and *(ii)*, letting *h* denote the spatial step in both directions *x* and *z,* while Δt is the time step. At the split node (i, j_0) and instant *t*, the application of central differences in time and operator **G** to (1.1) yields,

$$\begin{aligned}\left[\dot{u}_x^{\pm}(t+\Delta t/2)\right]_i &= \left[\dot{u}_x^{\pm}(t-\Delta t/2)\right]_i \\ &+ \frac{\Delta t}{\rho^{\pm}}\left\{\left[\tau_{xx'x}^{\pm}(t)\right]_i \pm \frac{g_{11}}{h}\left[\tau_{xz}^{*}(t)\right]_i \pm \frac{g_{12}}{h}\left[\tau_{xz}(t)\right]_{i,j_0\pm 1/2} \pm \cdots \pm \frac{g_{16}}{h}\left[\tau_{xz}(t)\right]_{i,j_0\pm 9/2}\right\},\end{aligned} \tag{20}$$

from which (via a second application of the central difference operator in time)

$$\left[u_x^{\pm}(t+\Delta t)\right]_i = \left[u_x^{\pm}(t)\right]_i + \Delta t\left[\dot{u}_x^{\pm}(t+\Delta t/2)\right]_i . \tag{21}$$

To emphasize the physical interpretation, and facilitate comparison with previous formulations (e.g., D05, DD07) we can rewrite (20) in the form of a force balance. In doing so, we identify

split nodal masses $M_i^{\pm} = \rho_i^{\pm} h^3 / 2$ at this location. Then we identify the terms in (20) involving stresses other than the fault-plane traction τ_{xz}^* as the restoring forces on the two parts of the split node, denoting them as $R_i^{\pm}$. Finally, in anticipation of applying the boundary conditions in terms of absolute stress levels, rewrite the fault-plane traction in terms of total shear traction T (instead of τ_{xz}^*, which is shear traction relative to its initial static equilibrium value). The result is that (20) takes the form

$$\left[\dot{u}_x^{\pm}(t+\Delta t/2)\right]_i = \left[\dot{u}_x^{\pm}(t-\Delta t/2)\right]_i + \Delta t \left(M_i^{\pm}\right)^{-1} \left\{ \left[R^{\pm}(t)\right]_i \pm \frac{g_{11} h^2}{2} \left[T(t) - \tau_{xz}^0\right]_i \right\}, \qquad (22)$$

where

$$M_i^{\pm} = \rho_i^{\pm} h^3 / 2 \qquad (23)$$

$$\left[R^{\pm}(t)\right]_i = \frac{h^3}{2} \left\{ \left[\tau_{xx,x}^{\pm}(t)\right]_i \pm \frac{g_{12}}{h} \left[\tau_{xz}(t)\right]_{i, j_0 \pm 1/2} \pm \cdots \pm \frac{g_{16}}{h} \left[\tau_{xz}(t)\right]_{i, j_0 \pm 9/2} \right\}, \qquad (24)$$

and

$$\left[T_i(t)\right]_i = \left[\tau_{xz}^*(t)\right]_i + \left[\tau_{xz}^0\right]_i . \qquad (25)$$

The origin of the change of sign on the τ_{xz} terms (i.e., the use of plus sign for R^+, minus sign for R^- in (24)) can be understood from the form of the **G** operator as shown in (16): the plus-side **G** differentiation operator at a split node uses the 6 coefficients g_{11}, ..., g_{16} at the beginning of the top row of $\mathrm{G}_{CG}^{(N)}$, whereas the minus-side differentiation uses the coefficients at the end of the bottom row of $\mathrm{G}_{CG}^{(M)}$, and because of the centro-skew symmetry (14), the latter are just the negatives of the former, arranged in reverse order.

The total trial traction $\tilde{T}_i$ that enforces zero slip velocity (i.e., $\dot{u}_x^+ = \dot{u}_x^-$) at time $t + \Delta t/2$ in equation (20) is

$$\left[\,\tilde{T}(t)\,\right]_i = \left[\tau_{xz}^0\right]_i + \kappa_i\left(\left[\,R^+(t)/M^+ - R^-(t)/M^-\right]_i - \frac{1}{\Delta t}\left[\,\dot{u}_x^+(t-\Delta t/2) - \dot{u}_x^-(t-\Delta t/2)\,\right]_i\right), \quad (26)$$

where

$$\kappa_i = \frac{2}{g_{11}h^2}\left[1/M^+ + 1/M^-\right]_i^{-1}. \quad (27)$$

This equation for $\tilde{T}_i$ represents the outcome of step *(i)* of the TSN method. Step *(ii)* sets a definite value of the total shear traction T_i that satisfies boundary conditions (4) and (5) and imposes the friction law (6) and (7),

$$\left[T(t)\right]_i = \begin{cases} \left[\tilde{T}(t)\right]_i & ;\ \left[\tilde{T}(t)\right]_i \le \tau_c \\ \tau_c\,\mathrm{sgn}\left[\tilde{T}(t)\right]_i \end{cases}. \quad (28)$$

Because the friction coefficient that determines τ_c is here taken to be slip dependent only, it can be updated explicitly, using (6) (with the normal stress at *i* approximated by $0.0625\left[-(\tau_{zz})_{i-3/2,j_0} + 9(\tau_{zz})_{i-1/2,j_0} + 9(\tau_{zz})_{i+1/2,j_0} - (\tau_{zz})_{i+3/2,j_0}\right]$). In the case of a friction coefficient dependent upon slip rate and one or more state variables, this step is more complicated, and MOSN updates the traction, slip velocity and state variables simultaneously at a given node, using an implicit solver (Rojas et al., 2007). Notice conditions (4) and (5) are fulfilled under either case that holds in equation (28). In particular, tangential velocity at $t + \Delta t/2$ is continuous when $\tilde{T}_i$ is less than the frictional strength τ_c. Substitution of $\left[T(t)\right]_i$ in (22) followed by the application of equation (21) allow the calculation of split displacements $\left[u_x^{\pm}(t+\Delta t)\right]_i$.

Finally, we calculate $\left[u_z^*(t+\Delta t)\right]_{i+1/2}$ from the condition of continuity of normal traction at the fault plane. This calculation follows closely the scheme of DD07, but using the mimetic differentiation formulas for all fault-normal derivatives and the standard staggered fourth- order

stencil for all fault-parallel derivatives. As in DD07, this step has to precede the determination of the split stress $\left(\tau_{xx}^{\pm}\right)_{i+1/2}$, since the latter calculation requires the z derivative of u_z at the fault plane.

Artificial viscosity

In order to attenuate spurious high-frequency oscillations observed in the numerical solutions of crack problems, artificial damping terms have been considered in finite differences (e.g., Day, 1982; Virieux & Madariaga, 1982; D05; DD07), finite elements (e.g., Oglesby et al., 1998), and finite volume (Ben Jemaa et al., 2007) methods. Numerical dispersion arises from the use of low-order spatial differentiation, and is a significant source of error in modeling abrupt stress drops experienced at the rupture fronts, which excite the short wavelengths most subject to dispersion. We expect less severe numerical dispersion from MOSN, compared with second-order methods, but we nonetheless explore the contribution of an artificial viscous damping in MOSN. Following D05, we compute damped stress terms of Kelvin-Voigt form $\left[\overline{\tau}_{xx}\right]_{i+1/2,j}$, $\left[\overline{\tau}_{zz}\right]_{i+1/2,j}$ and $\left[\overline{\tau}_{xz}\right]_{i,j+1/2}$ using the results from the discretized stress-strain relations (2). For instance,

$$\left[\overline{\tau}_{xx}\right]_{i+1/2,j} = \left[\tau_{xx}\right]_{i+1/2,j} + \eta \Delta t \left[\dot{\tau}_{xx}\right]_{i+1/2,j} . \tag{29}$$

Similar definitions apply to $\overline{\tau}_{zz}$ and $\overline{\tau}_{xz}$. Once calculated, $\overline{\boldsymbol{\tau}}$ replaces $\boldsymbol{\tau}$ in the discrete counterparts of equations of motion (1). The coefficient η is a dimensionless damping parameter whose effect on MOSN solutions will be discussed in later sections. This procedure represents a volumetric damping and its effect on the TSN computation is introduced through the restoring force terms. Equation (24) is rewritten in terms of damped stresses as,

$$\left[R^{\pm}(t)\right]_i = \frac{h^3}{2}\left\{\left[\overline{\tau}_{xx,x}^{\pm}(t)\right]_i \pm \frac{g_{12}}{h}\left[\overline{\tau}_{xz}(t)\right]_{i,j_0\pm 1/2} \pm \cdots \pm \frac{g_{16}}{h}\left[\overline{\tau}_{xz}(t)\right]_{i,j_0\pm 9/2}\right\}. \tag{30}$$

NUMERICAL TEST 1: KOSTROV'S PROBLEM

In this section, we present the first validation test of the MOSN algorithm by solving numerically the self-similar crack problem stated above (equations (1)–(3)). This test is similar to the one presented by Ben Jemaa *et al.*, 2007, where the medium corresponds to a Poisson solid (i.e., $\alpha/\beta = \sqrt{3}$) with α = 4000 m/s and the rupture velocity is set as $v_R = 0.5\alpha$. The domain is uniformly discretized in both directions x and z by a common grid interval h. Along the fault, a first receiver is placed at the point where the rupture initiates, followed by four more equidistant receivers (at 2 km intervals). Fig. 3 compares the MOSN time histories of slip and incremental shear stress at these locations with the corresponding time histories for the analytical solution. Both numerical and analytical slip histories have been scaled using the exact slip experienced at the first location (x = 0) over the time interval of the calculation (t = 5 s); and similarly, incremental stress fields are divided by the magnitude τ_{xz}^0, yielding a post-rupture level of -1. τ_{xz}^0 Figs 3a – 3c, show the effect of reducing h on the accuracy of the numerical solution, when no damping (η = 0) is used. As h decreases, MOSN solutions approach the analytical solutions, in both slip and shear stress fields. Figs 3a – 3c also show how grid refinement reduces the amplitudes of spurious oscillations, in the absence of numerical damping. Then Fig. 3d depicts the additional suppression of the spurious oscillations when a damping parameter of η = 0.1 is employed (with h = 50 m). The suppression of oscillations when using η>0 comes at the price of introducing a small (< 10%) increase in the misfit to the S wave stress peak that precedes rupture arrival. For the solution of more realistic, nonlinear problems (where strong coupling may occur among different frequency components of the solution), a judicious, case by case assessment of such tradeoffs is useful. Misfits for the Kostrov problem are summarized in quantitative form in Tables 1 and 2, for various combinations of grid spacing h and parameter η. Table 1 shows

relative RMS errors in slip histories at each of five receivers during the entire simulation (t = 5 s), and Table 2 summarizes relative RMS errors in truncated shear stress histories (in which the misfit calculation is truncated when the analytical stress drops to its minimum right after the S-wave arrival, to avoid the shear stress singularity).

NUMERICAL TEST 2: SPONTANEOUS RUPTURE

We next use the MOSN algorithm to model the spontaneous propagation of rupture along a finite fault, and the associated in-plane motion. The mathematical formulation for this problem corresponds to equations (1), (2), with boundary conditions stated in equations (4)-(7). Our test case represents a 2D analog of Version 3 of the Southern California Earthquake Center (SCEC) benchmark problem proposed by Harris *et al.* (2004). Fig. 4 depicts an elastic, homogeneous, and isotropic plane where rupture is allowed on a 30 km long fault segment along the x axis. Material properties are α = 6000 m/s, β = 3464 m/s, and ρ = 2670 kg/m^3. Distributions of the initial stress field and frictional parameters required in (6) and (7) are specified in Table 3. Nucleation occurs in a 3 km long patch centered on the fault where the initial shear stress exceeds the static yield stress by approximately 0.44%. Once it initiates, the rupture propagates bilaterally through the fault, governed by the fracture criterion (6) and (7). Beyond the fault segment, the static frictional strength is infinite and thus stops the further extension of the rupture.

Because this test problem lacks an analytical solution, we assess numerical results generated by the MOSN algorithm through comparison with a reference solution computed by the second-order accurate DFM algorithm (Day, 1982), the accuracy of which has been quantified by comparison with a boundary integral method (D05). We compare MOSN solutions against a high-resolution DFM solution (h = 0.0125 km) of the test problem, following the

comparison methodology introduced by D05. This reference solution is denoted as DFM0.0125 according to the notation used by D05 to distinguish among multiple-resolution solutions. We used artificial-viscosity parameter η=0.1 for the reference solution. However, the reference solution has no significant sensitivity to this parameter. This insensitivity is because, for a given η, the absorption-wavelength spectrum shifts in proportion to h (D05), and, in the case of our reference solution, h is (by design) far separated from the cohesive zone dimension (which in this test problem is the minimum dimension of physical significance). We name MOSN solutions using the same convention to designate the grid interval (given in km) employed in their computations; thus MOSN0.0375 denotes our numerical solution for h = 0.0375 km, for instance. Ten different approximations to our test case were calculated by the MOSN method by varying h from 0.0375 km to 0.5 km (see Table 4). The same grid size was used in both directions x and z.

Metrics

D05 proposed three error metrics for quantitative assessment of approximate solutions to dynamic rupture problems, relative to a reference solution: (i) root mean square (RMS) average of the rupture time differences, where rupture time is defined as the time at which slip velocity first exceeds 1 mm/s; (ii) RMS average of the differences in final slip, and (iii) RMS average of the differences in peak values of slip velocity. The rupture times are discrete time steps (but DD07 showed that further refining the rupture time estimates by taking much smaller time steps than required for stability does not significantly change the value of this metric as a function of spatial step h). In our test case, these metrics are calculated as sums over each grid point along the fault segment (-30 km < x < 30 km), for each MOSN solution with respect to the reference solution DFM0.0125. We report fractional values of these metrics relative to the RMS average

values of 2.93 s, 5.89 m, 6.59 m/s, for rupture time, final slip, and peak slip velocity, respectively (as given by DFM0.0125).

Solution dependence on damping parameter η

We first examine the effect of the artificial damping parameter η on dispersion and accuracy properties of the MOSN algorithm. Obviously, the larger the value of η, the smaller the amplitude of high-frequency oscillations in the numerical solution. However, over-damped solutions may poorly represent important features of the continuous solution like, for instance, maximum or minimum values. Metrics introduced above are used to determine a preferred value of η, at least for our test case. The test problem is solved using ten different grid intervals (h values are given in Table 4) and a range of values of η in the interval [0, 0.6]. Then, for each simulation corresponding to a pair (h, η), the two error metrics of rupture time and peak slip velocity are calculated. The final slip metric was not involved in this analysis, given its negligible sensitivity to small variations of the damping parameter η. This study parallels that presented in DD07, except that in the latter the general 3D Version 3 SCEC rupture problem (referred above) was solved and damped stress terms were used only in the TSN treatment of jump conditions.

Fig. 5(a) shows curves of RMS misfit in rupture time as a function of η, for each grid interval h. The accuracy of MOSN solutions in rupture time is only weakly dependent on η, especially for grid interval of h = 0.2 km or smaller, as indicated by RMS misfit curves that are almost parallel to the η - axis, with a slight decreasing pattern as η increases (slopes at η = 0.5 are approximately -0.03, -0.11, -0.08, -0.3, -0.29 and 0.4 for the case of h = 0.0375, 0.05, 0.075, 0.1, 0.15, and 0.2 km, respectively). On the other hand, for larger grid intervals (h ~0.3 km and

larger), precision worsens significantly as η increases constraining optimal values of η to a neighborhood of $\eta = 0.1$.

Fig. 5(b) shows the sensitivity of MOSN solutions to η, in terms of the peak slip rate metric. Error curves are visibly sensitive to the damping parameter even in the case of small grid sizes. For example, error increases by nearly a factor of 3 from 7.5% in the case of $\eta = 0$ to 19% at $\eta = 0.6$, when solutions using $h = 0.05$ km are considered. In addition, accuracy monotonically degrades with increasing η beyond 0.1, which suggests choosing a preferred η in the interval (0, 0.1]. This conclusion is consistent with the study above based on rupture times, and similar to the conclusions of D05 (who on the basis of the rupture-time metric preferred $\eta = \sim 0.1$), and we adopt a preferred value $\eta = 0.075$, which gives good results for both metrics. For this η value, and grid sizes up to 0.15 km, rupture-time error does not exceed 0.6% and peak slip rate error does not exceed 12.5% (see also Table 4).The similar behavior of DFM and MOSN with respect to the viscosity parameter is to be expected, as they use analogous volumetric viscous terms (in contrast to the surface viscosity term used in DD07, for example).

Effect of grid resolution on solution accuracy

In this section, we quantify the dependence of solution accuracy on the grid size h. A set of ten MOSN solutions are computed for the range 0.0375 km $\leq h \leq$ 0.5 km, using the preferred artificial damping parameter $\eta = 0.075$. Then, the error metrics of rupture time, peak slip rate, and final slip are calculated from these solutions, taking DFM0.0125 as the reference solution. For comparison, we also compute DFM solutions to our test problem, and their error metrics relative to DFM0.0125, for the same range of h (and, $\eta = 0.1$). Both schemes, MOSN and DFM, share the same time step Δt, for each grid size h, given by $\Delta t = 0.5h\alpha^{-1}$, where $\alpha = 6000$ m/s.

As discussed in, e.g., D05, a meaningful assessment of solution accuracy for this class of crack problems, in terms of grid spacing *h,* should relate *h* to an intrinsic length scale known as *cohesive zone length*. The cohesive zone is the portion of the fault plane behind the crack tip where the shear stress decreases from its static value to its dynamic value, and slip path-length l satisfies $0 \le l \le d_0$ (e.g. Ida, 1972). In the cohesive zone, shear stress and slip rate vary rapidly, and proper numerical resolution of those changes is crucial for capturing the maximum slip rates and rupture propagation speeds. Numerical accuracy is dependent on the number of grid points that discretize the cohesive zone, a quantity that D05 and DD07 call N_c, defined as the ratio of the width of the cohesive zone, Λ, to the grid interval h (i.e., $N_c = \Lambda/h$).

Because Λ varies as the rupture propagates, the problem solution yields a time series of values, N_{ci}, each a local measure of grid resolution. Fig. 6(a) shows results for DFM0.0125. The figure was constructed by plotting the rupture time (continuous line) and time at which shear stress first reaches its dynamic frictional value $\sigma_n \mu_d$ (dashed line), with the cohesive zone indicated by the filled area between those times (because of the problem symmetry, only 15km < x < 30km is shown). Fig. 6(b) depicts the corresponding sequence of values Λ_i. For comparison, we also calculate Λ_i for solutions DFM0.05, DFM0.1, MOSN0.05, and MOSN0.1, and these results are also shown in Fig. 6(b). As expected, the longer the rupture propagates, the smaller the cohesive zone (e.g., Andrews, 1976a), and therefore the more significant the inaccuracies in the determination of its size. For the same grid resolution, the algorithm MOSN yields more accurate values of Λ_i than does DFM, consistent with MOSN's higher accuracy in the determination of rupture times and shear stress (as discussed below).

We follow D05 and use the median of N_{ci} values along the in-plane axis, $\overline{N}_c$, as a global measure of cohesive zone resolution. From the reference solution DFM0.0125, excluding values

within the nucleation zone, we calculate a median value $\bar{\Lambda}$ = 0.258 km for our test problem, so $\bar{N}c$ =0.258/*h*.

We next examine the RMS misfits given by both MOSN and DFM solutions, and relate these errors to the median cohesive resolution $\bar{N}_c$. Misfits in rupture time, slip rate, and final slip, are respectively shown in Figs 7, 8, and 9, and summarized in Table 4. MOSN misfits are plotted in open symbols, while solid symbols are used for DFM misfits. Note that the abscissa has been double labeled to show both grid interval *h* (on the bottom) and corresponding $\bar{N}_c$ (on the top).

In Fig. 7, the regression line to MOSN misfits has slope of 0.97, practically parallel to the dotted line that scales the time steps used in all these calculations. That is, MOSN errors have, in this metric, a nearly linear dependence upon grid spacing *h*. MOSN yields rupture time misfits not larger than 1%, provided that the median cohesive resolution is at least $\bar{N}_c$ = 1, while $\bar{N}_c \geq$ 0.52 assures errors less than 2% in this metric (Table 4). On the other hand, achieving DFM errors (Table 4) as small as 1% demands a value for $\bar{N}_c$ approximately twice as large. In the case of a coarse grid, where *h* = 0.5 km and $\bar{N}c$ = 0.52, DFM misfits may be up 7%. However, for smaller grid sizes, MOSN loses its advantage relative to DFM, because the latter follows a super-linear dependence upon *h,* with average slope 1.53 (dashed line in Fig. 8) (which, incidentally, differs from the corresponding value of ~3 found for DFM in a 3D test in D05). Thus, DFM displays a faster convergence rate than MOSN, while MOSN remains more accurate than DFM for all $h \geq$ 0.05 km. ($\bar{N}_c$ <~6), and is thus more computationally efficient for resolution values in this range. If we take 1% as a representative target for solution accuracy in practical applications, MOSN achieves the target with *h* roughly twice as large ($\bar{N}_c$ half as large) as required for DFM.

Fig. 8 shows that MOSN and DFM have similar accuracy in slip rate, both algorithms having slip-rate errors less than 10% for $\overline{N}_c \geq 2.6$ ($h \leq 0.1$ km). In this metric, the errors of both methods show a considerable scatter from power laws in *h,* however. The best fitting power-law approximations (also shown in Fig. 8) are similar, with exponents 0.85 and 0.68, respectively, and the difference between these exponents does not appear to be significant, in light of the scatter. In fact, an equally valid characterization of the figure is that the errors stagnate at around 5%, and convergent behavior is not well demonstrated in this metric over the range of *h* available here.

Fig. 9 illustrates an interesting difference in the way that RMS misfits in final slip behave as grid spacing varies, in the cases of MOSN and DFM. In the range 0.0375 km $\leq h \leq$ 0.1 km, i.e., for a median cohesive resolution $\overline{N}_c \geq 2.6$, both algorithms yield almost undistinguishable misfits whose dependence on *h* is power law, and approximately linear (power-law exponents 1.14, and 1.28, respectively). Then, beyond $h = 0.1$ km, MOSN misfits increase with *h* following the same power law, at least for grid spacing not larger than 0.5 km ($\overline{N}_c \geq 0.5$). On the other hand, DFM misfits experience a transition in the range 0.1 km $< h <$ 0.2 km, i.e., $1.3 < \overline{N}c < 2.6$, where they grow more than linearly. Then, in the range 0.2 km $\leq h \leq$ 0.5 km, the DFM errors resume power law behavior, with slope 1.24, which indicates that DFM recovers its original order of convergence after the transition regime. As a last comparative comment, notice that for a median cohesive resolution of $\overline{N}_c \geq 3.5$, errors in this metric are less than 1% for both algorithms. However, when $\overline{N}_c = 1$ ($h = 0.25$ km), MOSN misfit is still small, about 3.3%, while DFM error reaches nearly 19%. Misfits in final slip for both algorithms are given in Table 4.

Waveform comparison

Figs 10, 11, and 12 compare DFM0.15 and MOSN0.15 time histories of slip rate, slip, and total shear stress, respectively. These time series correspond to the point P, located along the fault segment, 12.5 km away from the center of the nucleation patch (Fig. 4). No filtering process has been used on these signals, i.e., direct outputs from DFM and MOSN algorithms were plotted for the purpose of examining numerical artifacts (e.g., numerical dispersion). As shown in Table 4, the median cohesive resolution is $\overline{N}_c = 1.7$ in this case. However, attending to the physical contraction experienced by the cohesive zone as the rupture propagates, Λ is about 0.2 km when the crack reaches the point P (Fig. 6b). Therefore, the actual local resolution available across the cohesive zone at point P is $0.2/h \approx 1.3$ (little more than one grid point). Again, solution DFM0.0125 is used as a reference solution.

Slip rate time histories (Fig. 10) show the expected effects of anomalous numerical dispersion: a time shift of the post-rupture peak, and artificial oscillations following the peak. The discreteness of the rupture advance may be a further contributor to the artificial oscillations, the latter effect being most pronounced when the cohesive zone is poorly resolved. The inset plot in Fig. 10 shows the delayed arrival of the peak value of slip rate in the DFM0.15 solution relative to the reference solution DFM0.0125. Conversely, MOSN0.15 solution does not have a noticeable time shift of the peak value. To explore and quantify the behavior of this numerical artifact in the solutions given by both algorithms, MOSN and DFM, we measured these time shifts for the whole set of solutions computed for this problem. Relative to the reference peak value (4.28 s) given by DFM0.0125, time shifts are -0.1%, -0.17%, -0.2%, -0.2%, -0.1%, 1.9%, 0.7%, 1.6%, -0.05%, 1.2% in the case of MOSN solutions, for grid sizes h = 0.0375, 0.05, 0.075, 0.1, 0.15, 0.2, 0.25, 0.3, 0.375, and 0.5 km, respectively. Negative values represent earlier occurrences of the peak value, while positive values correspond to delayed arrivals. On the other

hand, DFM solutions yield relative time shifts of 0.04%, 0.5%, 1.4%, 1.8%, 2.7%, 5.8%, 5%, 6.8%, 6.5 %, and 9.9 %, for the same set of grid sizes. Together with Fig. 7, these results confirm that the numerical rupture velocity is influenced by the order of accuracy used in discretizing the fault boundary conditions. The rupture front travels slower (relative to the reference solution) in DFM solutions, for all $\overline{N}_c$ (at least in the range $0.5 \leq \overline{N}c \leq 6.9$). In contrast, in MOSN solutions the rupture speed is higher than in the reference solution in fine grids ($\overline{N}c \geq 1.7$), and lower in coarser grids ($\overline{N}c \leq 1.3$). These time shifts represent the cumulative effect of rupture velocity errors between the nucleation zone and point P; their magnitudes are consistent with the global misfits in rupture arrival times calculated along the whole fault (previously studied). MOSN errors in peak-velocity timing do not exceed 2%, which is also true for MOSN rupture time errors. Similarly, in the case of DFM solutions, both time shifts of the peak slip-rate and rupture time misfits are not greater than 10% (Table 4). Actually, the former follow a super linear increase with h (with average slope 1.72) that nearly coincides with the grid dependence of the latter (with average slope 1.53).

The other effect of numerical dispersion in the slip rate time series is the occurrence of spurious oscillations that follow the peak value, with rapidly-decreasing amplitudes (Fig. 10). The amplitude of the first (and largest) oscillation following the initial peak is 7.6 % of peak velocity in the case of MOSN0.15, compared with 12.9% for the DFM0.15 solution. The apparent frequencies of the oscillations correspond to S wavelengths (λ_S) of 1.8h, and 5h, respectively. Thus, this example suggests that MOSN preserves slip-velocity features with minimum wavelengths two to three times shorter than the minimum-wavelength features preserved by DFM. This behavior corresponds roughly to differences in numerical dispersion expected (in linear wave propagation) on the basis of the order of accuracy used in the spatial

discretization, fourth order in the case of MOSN, and second order for DFM. Finally, note that the timing and shape of stopping phases coming back from the two ends of the fault segment, and arriving at point P between 5 s and 6 s, are significantly better modeled in MOSN0.15 than in DFM0.15.

Fig. 11 shows the almost indistinguishable MOSN0.15 and DFM0.15 time histories for the slip recorded at point P. The agreement of these approximations to the reference solution is nearly perfect, until they show a common discrepancy beginning at the time that stopping phases from the locked edges of the cracked fault reach point P (between, 5.5 s – 6 s). This kind of discrepancy in slip time series is common in rupture models with abrupt termination of the fault (DD07): because one grid interval separates the last grid point of the fault (at which slip is allowed) to the first grid point of the unbreakable medium (at which the fault is locked), an order h uncertainty on the specific point at which rupture ceases induces an ambiguity of the same order in the stopping-phase delays.

Shear stress time histories given by MOSN0.15 and DFM0.15 replicate each important feature seen in the reference solution, with the MOSN algorithm showing a modest improvement over DFM. In the magnified inset of the stress field (Fig. 12), critical values (either, maximum, or, minimum) reached by the reference solution are better reproduced by the MOSN scheme. For example, the first maximum (7.2 MPa increase above the initial stress level) is approximated by MOSN (6.9 MPa increase) with a relative error of about 4%, while the DFM approximation (5.9 MPa increase) has relative error of ~18%.

DISCUSSION AND CONCLUSIONS

We have developed a split-node finite difference method for modeling shear ruptures that is consistently fourth-order accurate in its spatial discretization, both in the interior of the

model and at the fault. The medium properties and elastic fields are discretized on a staggered grid with (apart from the fault) stresses and displacements at different points. The fault plane is discretized with split nodes that combine displacement and stress components at the same point, permitting all displacement and stress components to be located exactly along the fault plane. Consistent fourth-order accuracy is achieved through the use of mimetic operators and split nodes (MOSN). The former facilitate the one-sided numerical differentiation (in the fault-normal direction) that is required to preserve fourth-order accuracy in the presence of the discontinuities at the fault plane. The latter allows a natural representation of the fault discontinuity. Furthermore, the traction-at-split-node (TSN) formulation, i.e., coincident location of auxiliary shear-traction points at the split nodes, arises naturally within the staggered-grid mimetic framework when it is applied to a displacement discontinuity.

We have evaluated the MOSN method for two test problems entailing Mode II rupture propagation: the case of the propagation of a fixed-speed rupture (Kostrov's problem), and the case of a spontaneous rupture with slip-dependent friction. In the former case, the convergence of numerical results to the analytical solution through grid refinement was shown by consistently decreasing RMS misfits on slip and shear stress (avoiding singularities) time series. In the latter case, we examined waveform characteristics and analyzed convergence using quantitative metrics. Compared with the second-order DFM method, slip-velocity waveforms from MOSN solutions show significant reduction in artifacts attributable to numerical dispersion, giving improved timing of stress and slip-velocity peaks and stopping phases, while substantially reducing the spurious oscillations of slip velocity that are characteristic of low-order FD solutions.

The convergence analysis revealed a linear dependence of MOSN errors on the grid size. This implies a slow convergence of this fourth-order method on fine grids. Somewhat

paradoxically, this means that MOSN is significantly more accurate than our second-order comparison code (DFM) for relatively coarse grids, but loses this advantage for very fine grids. If we take 1% accuracy in the rupture time metric to be a reasonable standard for practical application of the methods, MOSN has a considerable advantage, reaching the target accuracy with grid spacing h approximately twice as large as required by DFM (though MOSN has no comparable advantage for the slip-velocity metric). This result, combined with the reduced post-rupture slip-velocity oscillations in MOSN solutions, mean that from a practical standpoint we have significant gains from the fourth-order formulation of MOSN. However, the poorer convergence relative to DFM, and its inability to improve the second-order results in the limit of small grid intervals, raises additional issues.

A potential reason for this behavior is the presence of gradient discontinuities in the linear slip-weakening (SW) friction law at zero slip and when the sliding equals the SW distance. These singularities in the friction model may introduce other high-order singularities in elastic fields around the evolving rupture (Ida, 1972), which would conflict with smoothness assumptions that are implicit in order-of-accuracy estimates for FD (and other) schemes. Preliminaries results of this paper therefore do not necessarily imply that finite-difference methods are limited to low-order accuracy when dealing with rupture problems. It may be that the potential benefits of high-order finite-difference methods will be more fully realized with the consideration of friction models with smooth evolution in terms of slip or slip rate. Examples of constitutive laws with these characteristics are the experimentally-based rate- and state-dependent class of friction models (Ruina, 1983; Dietrich, 1986), and the laboratory-derived slip-dependent model of Ohnaka and Shen, 1999**.** A common feature of these models is an initial re-strengthening stage where friction evolves smoothly respect to slip (e.g., Bizarri *et al.*, 2001). In particular, frictional traction governed by rate- and state-dependent models have an initial

velocity-strengthening stage that should ensure smoothness. We are currently examining convergence rates of MOSN with such models to assess the hypothesis that non-analyticity in the slip-dependent friction law is responsible for the apparent low-order convergence of MOSN. We are also examining a second factor that may contribute to the low convergence rate, which is the possibility that convergence is limited principally by the time discretization, which is second-order, rather than by the spatial discretization.

The current implementation of MOSN for two dimensions and Cartesian meshes, with a planar fault, can be seen as a first step towards the exploitation of high-order operators in finite difference rupture modeling. Accuracy and stability showed by MOSN in solving two in-plane crack problems leads us to note several possible generalizations of this method. First, MOSN could be extended to 3D domains and planar faults, using as a basis the successful adaptation of the TSN method to a 3D SSG introduced by DD07. An alternative effort may be focused in adapting MOSN to 2D or 3D curvilinear coordinates, allowing the solution of faulting boundary conditions along non-straight faults. Finally, while MOSN introduces 1D mimetic operators as a component of a 2D solution, we note that there are fully 2D (or 3D) mimetic formulations (i.e., FD discretizations that preserve the multi-dimensional adjoint relations between divergence and gradient) in the second order case (e.g., Hyman *et al.*, 1997), and these have been applied to the rupture dynamics problem by Ely (2007). Generalization of those fully multidimensional mimetic formulations to fourth order (or higher), while possible in principle, presents rather formidable technical complications (Ely, 2007), however, compared with the use of the 1D operators proposed here, and the benefits would need to be weighed carefully against alternative formulations (e.g., spectral element, finite volume, discontinuous Galerkin, etc) that may offer comparable order of accuracy.

ACKNOWLEDGMENTS

Authors thank Dr. J. Virieux and his group for providing analytical results for the fixed-speed shear crack problem. We also thank Dr. Kim Olsen for his helpful comments, and thank Jean Paul Ampuero and an anonymous reviewer for very thorough and helpful reviews. This work was supported by the National Science Foundation, under grants ATM-0325033 and EAR-0623704, and by the Southern California Earthquake Center (SCEC). SCEC is funded by NSF Cooperative Agreement EAR-0529922 and USGS Cooperative Agreement 07HQAG0008. Otilio J Rojas was also funded by Universidad Central de Venezuela (CDCH). The SCEC contribution number for this paper is 1084.

REFERENCES

Aagaard, B., Heaton, T., & Hall, J., 2001. Dynamic earthquake ruptures in the presence of lithostatic normal stresses: Implications for friction models and heat production, *Bull. Seism. Soc. Am.,* 91, 1765-1796.

Ampuero, J. P., 2002. Etude physique et numerique de la nucleation des seismes, Doctoral thesis, University of Paris.

Andrews, D., 1973. A numerical study of tectonic stress release by underground explosions, *Bull. Seism. Soc. Am.,* 63, 1375-1391.

Andrews, D., 1976a. Rupture propagation with finite stress in antiplane strain, *J. Geophys. Res., 81*, 3575-3582.

Andrews, D., 1976b. Rupture velocity of plane-strain shear cracks, *J. Geophys. Res.*, 81, 5679-5687.

Andrews, D., 1999. Test of two methods for faulting in finite-difference calculations, *Bull. Seism. Soc. Am.*, 89, 931-937.

Archuleta, R. & Day, S. M., 1980. Dynamic rupture in a layered medium: the 1966 Parkfield earthquake, *Bull. Seism. Soc. Am.,* 708, 671-689.

Ben Jemaa, M., Glinsky, N., Cruz-Atienza, V., Virieux, J. & Piperno, S. Dynamic non-planar crack rupture by a finite volume method. *Submitted to Geophys. J. Int.*, *(January 2007).*

Bizarri, A., Cocco, M., Andrews, D., & Boshi, E. 2001. Solving the dynamic rupture problem with different numerical approaches and constitutive laws, *Geophys. J. Int.*, 144, 656-678.

Burridge, R. & Willis J. R., 1969. The self-similar problem of the expanding elliptical crack in an anisotropic solid*, Proc. Cambr. Phil. Soc.*, 66, 443-468.

Broberg, K. B., 1999. Cracks and Fracture*,* pp. 45-48, Academic Press, London.

Castillo, J. & Grone, R., 2003. A matrix analysis approach to higher-order approximations for divergence and gradients satisfying a global conservation law. *SIAM J. Matrix Anal. Appl.*, 25, 128-142.

Castillo, J., Hyman, J., Shashkov, M. & Steinberg, S., 2001. Fourth- and sixth-order conservative finite difference approximations of the divergence and gradient. *Appl. Numer. Math.*, 37, 171-187.

Dalguer, L. A. & Day, S. M., 2006. Comparison of fault representation methods in finite difference simulations of dynamic rupture, *Bull. Seism. Soc. Am.*, 96, 1764-1778.

Dalguer, L. A., Day, S. M., Olsen, K. B. & Cui, Y., 2006. Implementation of the staggered-grid split-node method in a MPI finite difference code for large scale models of spontaneous dynamic rupture simulation (abstract), *Annual Meeting of Southern California Earthquake Center (SCEC), Proceedings and abstracts 2006*, Sept. 9-14, Palm Springs, California, p. 88.

Dalguer, L. A. & Day, S. M., 2007. Staggered Split Nodes Fault Model for Spontaneous Dynamic Rupture Simulation. *J. Geophys. Res.,* 112, B02302, doi:10.1029/2006JB004467.

Day, S. M., 1977. Finite element analysis of seismic scattering problems, Ph.D. dissertation, Univ. of Calif., San Diego.

Day, S. M., 1982. Three-dimensional simulation of spontaneous rupture: The effect of nonuniform prestress. *Bull. Seism. Soc. Am.*, Vol. 72, 1881-1902.

Day, S. M., Dalguer, L. A., Lapusta, N. & Liu, Y., 2005. Comparison of finite difference and boundary integral solutions to three-dimensional spontaneous rupture, *J. Geophys. Res.*, 110, B12307, doi:10.1029/2005JB003813.

Dieterich, J. H., 1979. Modeling of rock friction—1.Experimental results and constitutive equations*, J. Geophys.Res., 84*, 2161–2168.

Dieterich, J. H., 1986. A model for the nucleation of earthquake slip, in *Earthquake Source Mechanics*, *Geophysical Monograph*, Vol. 37, Maurice Ewing Ser. 6, pp. 37-47, eds Das, S., Boatwright, J. & Scholz, C. H., AGU, Washington DC.

Ely, G., Minster, B. & Day, S. M., 2006. Large scale dynamic rupture modeling with realistic geometry, *Annual Meeting of Southern California Earthquake Center (SCEC), Proceedings and abstracts*, Sept. 9-14, 2006, Palm Springs, California, p. 94.

Ely, G. P., Day, S. M. & Minster, J. B., 2007. A support-operator method for viscoelastic wave modeling in 3D heterogeneous media, *Geophys. J. Int.* , in review.

Festa, G., and Vilotte, J.-P., 2006. Influence of the rupture initiation on the intersonic transition: Crack-like versus pulse-like modes, *Geophys. Res. Lett.,* Vol 33, L15320, doi:10.1029/2006GL026378.

Harris, R., Archuleta, R., Aagaard, B., Ampuero, J., Andrews, J., Dalguer, L., Day, S. M., Dunham, E., Ely, G., Kase, Y., Lapusta, N., Liu, Y., Ma, S., Oglesby, D., Olsen, K. & Pitarka, A., 2004. The source physics of large earthquakes: Validating spontaneous rupture methods, *EOS Trans. AGU*, 85(47), Fall Meet. Suppl., Abstract S12A-05.

Hyman, J., Shashkov, M. & Steinberg, S., 1997. The numerical solution of diffusion problems in strongly heterogeneous non-isotropic materials. *J. Comput. Phys.*, 122, 130-148.

Hyman, J. & Shashkov, M., 1999. Mimetic discretization for Maxwell's equations, *J. Comput. Phys.*, 151, 881-909.

Hyman J., Morel, J., Shashkov, M. & Steinberg, S., 2002. Mimetic finite difference methods for diffusion equations, *Comput. Geosci.*, 6, 333-352.

Ida, Y., 1972. Cohesive force across the tip of a longitudinal-shear crack and Griffith's specific surface energy. *J. Geophys. Res.,* 77, 3796-3805.

Kaneko, Y., Lapusta, N. & Ampuero, J. P., 2006. Spectal element modeling of earthquake nucleation and spontaneous rupture on rate and state faults. *Annual Meeting of Southern California Earthquake Center (SCEC), Proceedings and abstracts 2006*, Sept. 9-14, Palm Springs, California, p. 112.

Kostrov, B.V., 1964. Self-similar problems of propagation of shear cracks, *J. Appl. Math. Mech.* 28, 1077-1087. English translation from PMM, 28 (1964), 889-898.

Kristek, J., Moczo, P. & Archuleta, R., 2002. Efficient methods to simulate planar free surface in the 3D 4^{th}-order staggered-grid finite-difference schemes. *Stud. Geophys. Geod.*, 46, 355-381.

Kristek, J., Moczo, P. & Galis, M., 2006. Comparison of the 2nd-order and 4th-order staggered-grid finite-difference implementations of the TSN method for rupture propagation. *Eos Trans. AGU*, 87(52), Fall Meet. Suppl., Abstract S41C-1341.

Levander, A., 1988. Fourth-order finite-difference P-SV seismograms. *Geophysics*, 53, 1425-1436.

Graves, R., 1996. Simulating seismic wave propagation in 3D elastic media using staggered-grid finite differences, *Bull. Seism. Soc. Am.*, 86, 1091-1106.

Madariaga, R., 1976. Dynamics of an expanding circular fault. *Bull. Seism. Soc. Am.* 66 639-666.

Madariaga, R., Olsen, K. & Archuleta, R., 1998. Modeling dynamic rupture in a 3D earthquake fault model. *Bull. Seism. Soc. Am.*, Vol. 88, 1182-1197.

Madariaga, R., Ampuero, J. P., Adda-Bedia, M., 2006. Seismic radiation from simple models of earthquakes, in *Radiated Energy and the Physics of Earthquakes*, *Geophysical Monograph Series, Vol. 170*, edited by A. McGarr, R. Abercrombie, H. Kanamori, and G. di Toro, American Geophysical Union.

Moczo, P., Kristek, J., Vavrycuv, V., Archuleta, R. & Halada, L., 2002. 3D heterogeneous staggered-grid finite-difference modeling of seismic motion with volume harmonic and arithmetic averaging of elastic moduli and densities, *Bull. Seism. Soc. Am.*, 92, 3042-3066.

Moczo, P., Robertsson, J. O. A. & Eisner, L., 2006. The finite-difference time-domain method for modeling of seismic wave propagation, in *Advances in Wave Propagation in Heterogeneous Earth*, Advances Geophysics series, edited by R.-S. Wu and V. Maupin, chap. 8, Elsevier, New York.

Moczo, P., Kristek, J., Galis, M., P., Pazak & Balazovjech, M., 2007. The finite-difference and finite-element modeling of seismic wave propagation and earthquake motion, in *Acta Physica Slovaca*, 52(2), 177-406.

Olsen, K., Day, S. M., Minster, B., Cui, Y., Chourasia, A., Faerman, M., Moore, R., Maechling, P. & Jordan, T., 2006. Strong Shaking in Los Angeles Expected From Southern San Andreas Earthquake, *Geophys. Res. Lett.*, 33, L07305, doi:10.1029/2005GRL025472.

Oglesby, D., Archuleta, R. & Nielsen, S., 1998. Earthquakes on dipping faults: The effects of broken symmetry, *Science*, 280, 1055-1059.

Ohnaka, M. & Shen, L., 1999. Scaling of the shear rupture process from nucleation to dynamic propagation: implications of geometric irregularity of the rupturing surfaces, *J. Geophys.*

Res., 104, 817-844.

Palmer, A. & Rice, J., 1973. The growth of slip surfaces in the progressive failure of overconsolidated clay slopes, *Proc. R. Soc. London, Ser. A*, 332, 537.

Pitarka, A., 1999. 3D finite-difference modeling of seismic motion using staggered grids with nonuniform spacing, *Bull. Seism. Soc. Am.*, 89, 54-68.

Rice, J., 2006. Heating and weakening of faults during earthquake slip, *J. Geophys. Res.*, 111, B05311, doi:10.1029/2005JB004006.

Richards, P. G., 1973. The dynamic field of a growing plane elliptical shear crack, *Int. J. Solid Structures*, 9, 843-861.

Richards, P. G., 1976. Dynamic motions near an earthquake fault: a three-dimensional solution *Bull. Seism. Soc. Am.*, 66, 1-32.

Ruina, A., 1983. Slip instability and state variable friction laws, *J. Geophys. Res*., 88, 10359-10370.

Rojas, O., Day, S. M., Castillo, J. & Dalguer, L., 2006. Modeling of rupture propagation using high-order mimetic finite-differences. *Annual Meeting of Southern California Earthquake Center (SCEC), Proceedings and abstracts 2006*, Sept. 9-14, Palm Springs, California, p. 153.

Rojas, O., Day, S. M., Castillo, J. & Dalguer, L., 2007. High-order modeling of rupture propagation using different constitutive laws. *SSA 2007 Annual Meeting Abstracts,* Hawaii, USA.

Shashkov, M. & Steinberg, S., 1996. Solving diffusion equations with rough coefficients in rough grids, *J. Comput. Phys.*, 129, 383-405.

Strand, B., 1999. Simulations of acoustic wave phenomena using high-order finite difference approximations, *SIAM J. Sci. Comput.*, 20, 1585-1604.

Virieux, J., & Madariaga, R., 1982. Dynamic faulting studied by a finite difference method, *Bull. Seism. Soc. Am.*, 72, 345-369.

Virieux, J., 1986. P-SV wave propagation in heterogeneous media: Velocity-stress finite-difference method, *Geophysics*, 51, 889-901.

FIGURE LEGENDS

Figure 1. Uniform grid for staggered differentiation of functions *f* and *v* using the difference operators **D** and **G** (constructed in Equation 16 from Castillo-Grone operators $D_{CG}^{(K)}$ and $G_{CG}^{(K)}$). The node $z_0 = 0$ is split to accommodate a possible discontinuity of function *v*. Locations of vector components $\mathbf{v} = \left(v(z_{-M}),...,v^-,v^+,...,v(z_N)\right)$ and $\mathbf{f} = \left(f(z_{-M}),...,f_0,f_0,...,f(z_N)\right)$ are depicted. Quantities $(\mathbf{Dv})_{j+1/2}$ and $(\mathbf{Gf})_j$, (*j* integer) represent the approximations to *dv/dz* and *df/dz* calculated using operators **D** and **G**, respectively.

Figure 2. Two-dimensional staggered grid used to discretize medium parameters and wave-field variables. Grid points located along the fault plane (double line at *z* = 0) are split into a plus (+) half point and a minus (-) half point to allow the TSN implementation of faulting boundary conditions. Extra evaluations of shear stress τ_{xz}^* and vertical displacement u_z^* are placed at the fault plane to permit the approximation of $\tau_{xz,z}$ and $u_{z,z}$ using the mimetic operator **G**. Apart from the split nodes and extra fault-plane function evaluations (as also used in DD07), this grid is the Standard Staggered Grid (SSG) (Madariaga, 1976; Virieux and Madariaga, 1982).

Figure 3. MOSN solutions (circles) to the Kostrov problem are compared with analytical-solution time series (lines). Figures 3(a) – 3(c), show the gain in accuracy of the numerical solution as spatial step *h* is reduced and the consequent reduction of spurious oscillations . RMS misfits in both slip and shear stress time histories are reported in Tables 1 and 2. Figures 3(d) shows the damping of high-frequency oscillations achieved by using a convenient artificial damping parameter ($\eta = 0.1$), which also leads to a gain in accuracy on slip results (see Table 1)

Figure 4. Two dimensional fault model for testing spontaneous rupture propagation. The thick line in the center represents the 3km long nucleation patch. The triangle corresponds to the receiver P located on the fault plane, 12.5 km from the center of the nucleation patch. At this location, time series of shear stress, slip rate, and slip are recorded and analyzed. Stress and frictional parameters for this fault model are given in Table 3.

Figure 5. (a) RMS rupture time misfits as a function of the artificial damping parameter η for different grid sizes h. **(b)** RMS peak slip rate misfits as a function of the artificial damping parameter η for different grid sizes h. In both cases, misfits are calculated along the whole 30 km long fault using DFM0.0125 as a reference solution.

Figure 6(a). Cohesive-zone development during rupture propagation. Reference solution DFM0.0125 has been used to approximate both rupture time (continuous line) and the later time when shear stress reaches its dynamic yielding stress (dashed line) equal to $\tau_d = -\mu_d * \sigma_n$ (see Table 3). **6(b).** Size of the cohesive-zone as the rupture propagates in the interval [16.5, 30] Km (outside of the nucleation zone). Results using the reference solution DFM0.0125 (continuous line) are compared with those calculated from coarser-grid solutions DFM0.05, DFM0.1, MOSN0.05, and MOSN0.1. In both cases, only results for the right-half of the fault are shown due to the symmetry of the solution with respect to the center of the nucleation zone,.

Figure 7. Rupture time misfits, relative the reference solution DFM0.0125, as a function of the grid size h. Differences are RMS averages along the 30 km long fault. Open circles are MOSN errors which follow a slope of 0.97. Filled circles represent DFM errors which follow a slope of 1.53. The dashed line shows the dependence of time step Δt on h.

Figure 8. Peak slip rate misfits, relative the reference solution DFM0.0125, as a function of the grid size h. Differences are RMS averages along the 30 km long fault. Open diamonds are MOSN errors, filled diamonds are DFM errors. Regression lines for MOSN (slope 0.85) and DFM (slope 0.68) are also shown.

Figure 9. Misfits in final slip, relative the reference solution DFM0.0125, as a function of the grid size h. Differences are RMS averages along the 30 km long fault. Open squares are MOSN errors which follow a single line of slope of 1.14. Filled squares are DFM errors which follow, except for a transitional interval 0.1 km $< x <$ 0.2 km, nearly the same slope (1.28 for $x \leq 0.1$ and 1.24 for $x \geq 0.2$ km).

Figure 10. Slip rate time histories at the fault plane point **P** marked in Figure 4. Solutions MOSN0.15 and DFM0.15 are compared with the reference solution DFM0.0125.

Figure 11. Slip time histories at the fault plane point **P** marked in Figure 4. Solutions MOSN0.15 and DFM0.15 are compared with the reference solution DFM0.0125.

Figure 12. Shear stress time histories at the fault plane point **P** marked in Figure 4 Solutions MOSN0.15 and DFM0.15 are compared with the reference solution DFM0.0125.

TABLES

Table 1. Relative misfits of MOSN slip time histories at 5 receivers in a fixed-speed rupture simulation (Kostrov's problem)

h (m)	η	RMS (%) at x = 0	RMS (%) at x = 2 km	RMS (%) at x = 4 km	RMS (%) at x = 6 km	RMS (%) at x = 8 km
50	0	0.37	0.41	0.62	1.09	2.50
100	0	0.73	0.86	1.27	1.94	4.12
200	0	1.48	1.71	2.29	3.44	6.89
50	0.1	0.26	0.38	0.50	0.52	1.06
50	0.15	0.29	0.42	0.54	0.57	1.13
50	0.2	0.33	0.46	0.60	0.65	1.28
50	0.25	0.37	0.50	0.66	0.75	1.46

Table 2. Relative misfits for truncated MOSN shear stress time histories at 4 receivers in a fixed-speed rupture simulation (Kostrov's problem)

h (m)	η	RMS (%) at x = 2 km	RMS (%) at x = 4 km	RMS (%) at x = 6 km	RMS (%) at x = 8 km
50	0	18.9	10.5	8.38	7.38
100	0	25.7	18.9	13.6	10.5
200	0	44.7	25.7	23.6	18.9
50	0.1	19.4	11.4	10.1	8.16
50	0.15	20.8	13.1	11.6	9.33
50	0.2	22.2	14.7	13.1	10.5
50	0.25	23.6	16.2	14.3	11.5

Table 3: Dynamic Stress and Frictional Parameters for Spontaneous Rupture Simulation

Parameters	**Within fault segment of 30 km**		**Outside fault**
	Nucleation	**Outside nucleation**	**segment**
Initial shear stress τ_0, MPa	81.6	70.0	70.0
Initial normal stress $-\sigma_n$, MPa	120.0	120.0	120.0
Static friction coefficient μ_s	0.677	0.677	infinite
Dynamic friction coefficient μ_d	0.525	0.525	0.525
Static yielding stress $\tau_s = -\mu_s * \sigma_n$, MPa	81.24	81.24	infinite
Dynamic yielding stress $\tau_d = -\mu_d * \sigma_n$, MPa	63.0	63.0	63.0
Dynamic stress drop $\Delta\tau = \tau_0 - \tau_d$, MPa	18.6	7.0	7.0
Strength excess $\tau_s - \tau_0$, MPa	-0.36	11.24	infinite
Critical slip distance d_0, m	0.40	0.40	0.40

Table 4: Relative Misfits for MOSN and DFM Solutions in a Spontaneous Rupture Simulation

Spatial and time steps		**Median resolution**	**RMS rupture time misfits (%)**		**RMS peak slip rate misfits (%)**		**RMS final slip misfit (%)**	
Δt (s)	h (km)	$\overline{Nc}$	MOSN	DFM	MOSN	DFM	MOSN	DFM
3.1e-03	0.0375	6.88	0.14	0.12	4.61	6.53	0.348	0.356
4.2e-03	0.05	5.16	0.20	0.23	6.65	6.88	0.519	0.539
6.3e-03	0.075	3.44	0.28	0.48	7.65	7.23	0.858	0.902
8.3e-03	0.1	2.58	0.38	0.82	6.96	6.51	1.206	1.26
1.3e-02	0.15	1.72	0.59	1.45	12.5	11.1	1.893	3.51
1.7-02	0.2	1.29	0.74	2.22	20.4	16.7	3.182	13.3
2.1e-02	0.25	1.03	0.96	2.90	26.6	21.3	3.263	18.6
2.5e-02	0.3	0.86	0.99	3.65	30.6	24.1	3.95	25.8
3.1e-02	0.375	0.68	1.45	4.88	32.2	26.3	4.98	32.2
4.2e-02	0.5	0.52	1.79	6.95	32.9	29.2	6.74	41.1

Figure 1.

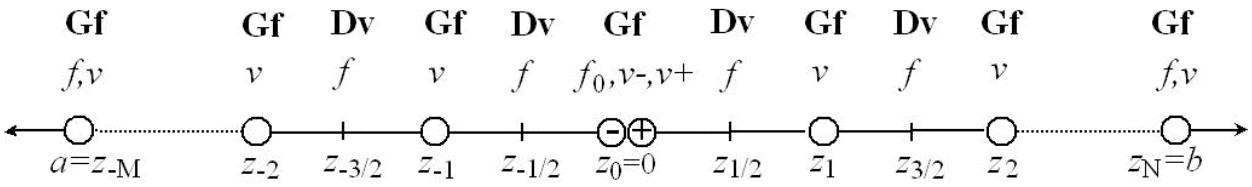
Gf
Gf
Dv
Gf
Dv
Gf
Dv
Gf
Dv
Gf
Gf
f,v
v
f
v
f
f0,v-,v+
f
v
f
v
f,v
a=z-M
z-2
z-3/2
z-1
z-1/2
z0=0
z1/2
z1
z3/2
z2
zN=b

Figure 2.

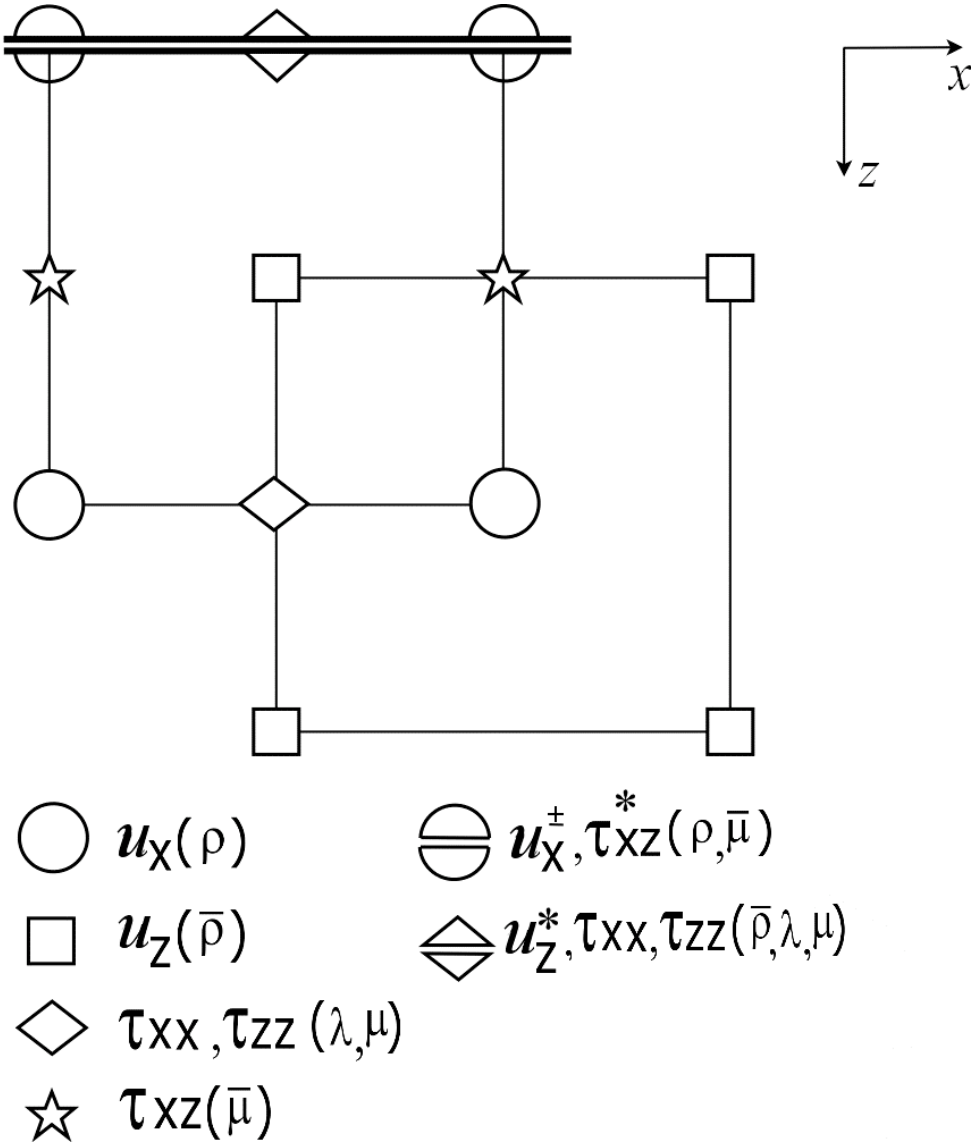
x
z
$u_x(\rho)$
$u_z(\bar{\rho})$
$\tau_{xx}, \tau_{zz}(\lambda,\mu)$
$\tau_{xz}(\bar{\mu})$
$u_x^{\pm}, \tau_{xz}^{*}(\rho,\bar{\mu})$
$u_z^{*}, \tau_{xx}, \tau_{zz}(\bar{\rho},\lambda,\mu)$

Figure 3(a)

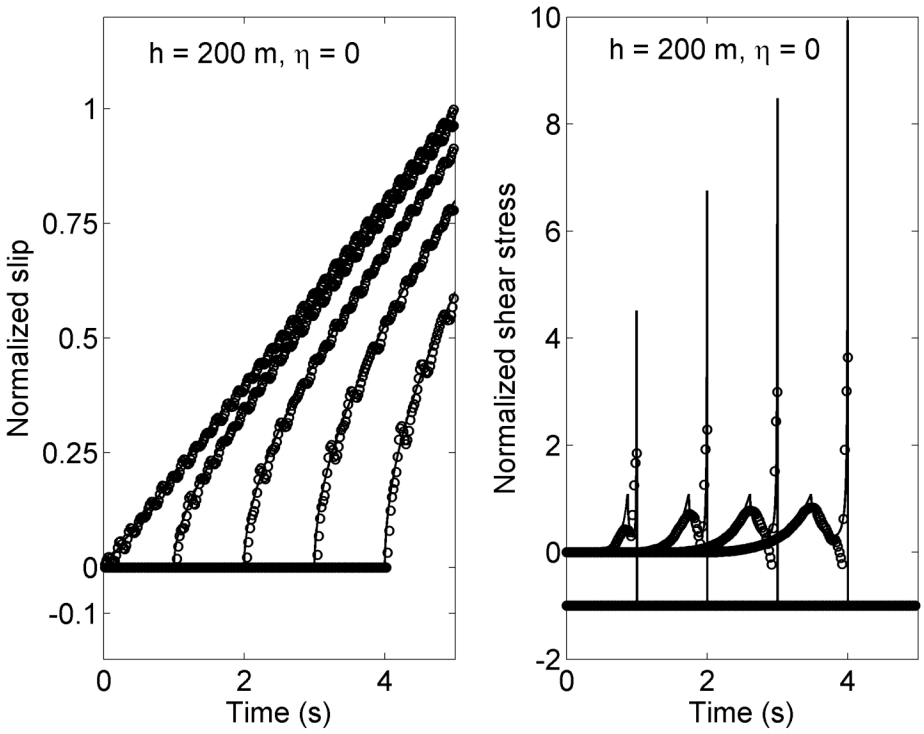

Figure 3(b)

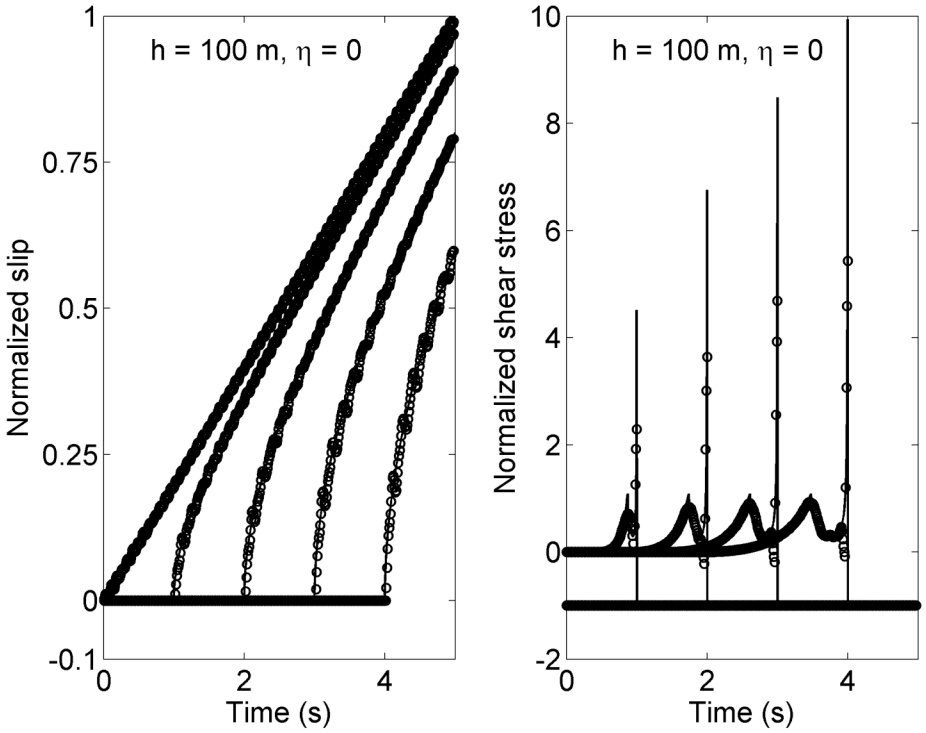

Figure 3(c)

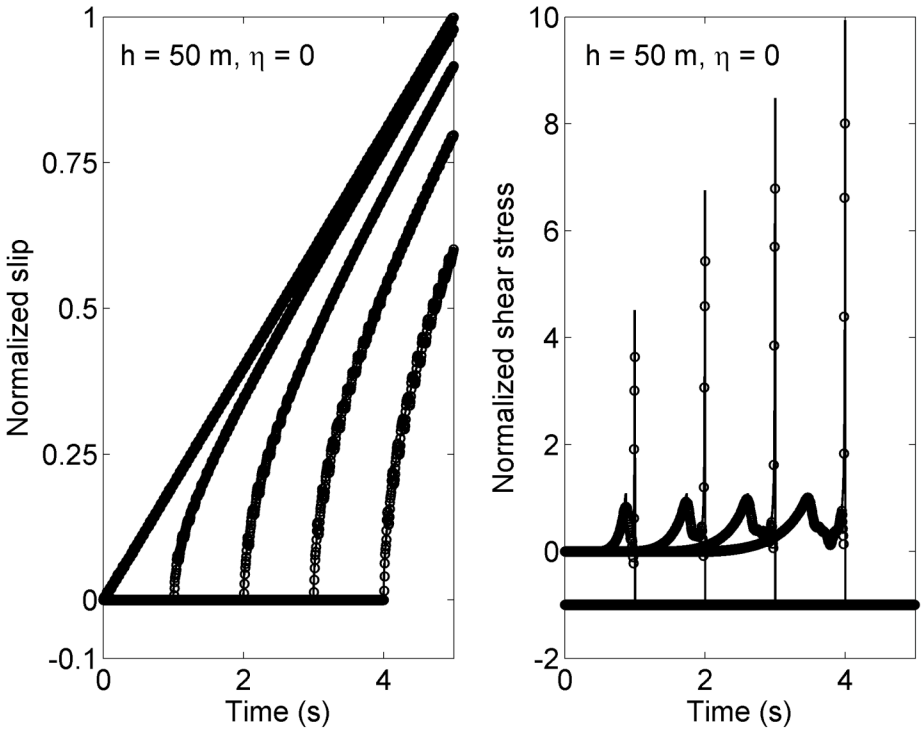

Figure 3(d)

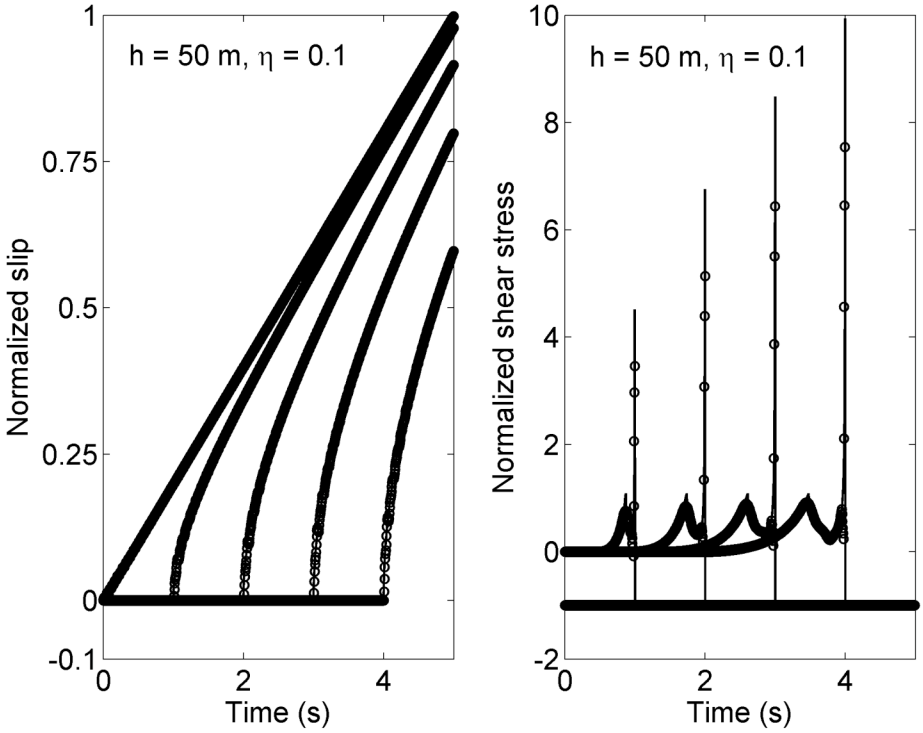

Figure 4.

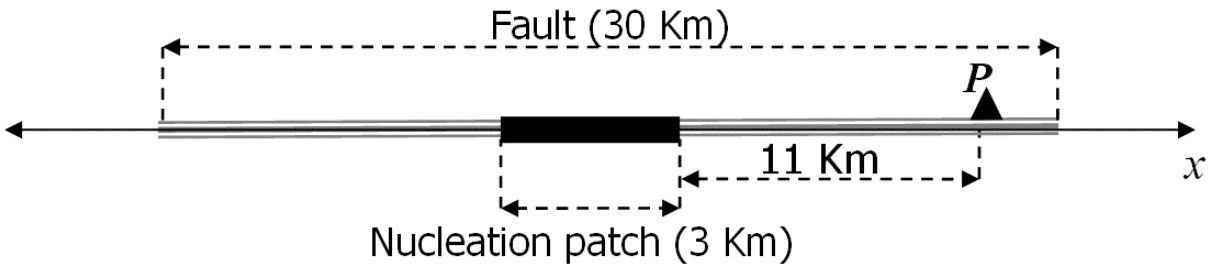

Figure 5(a).

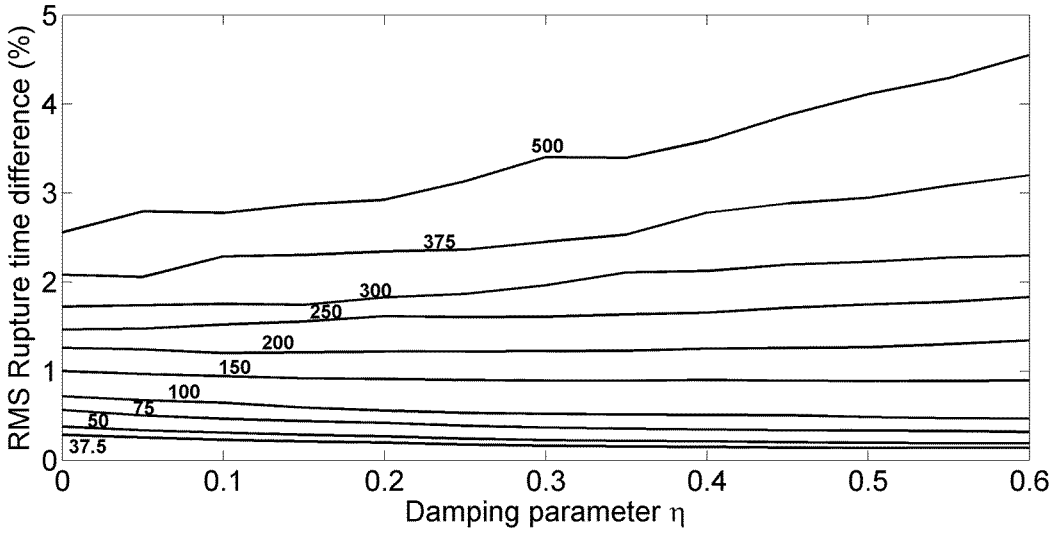

Figure 5(b).

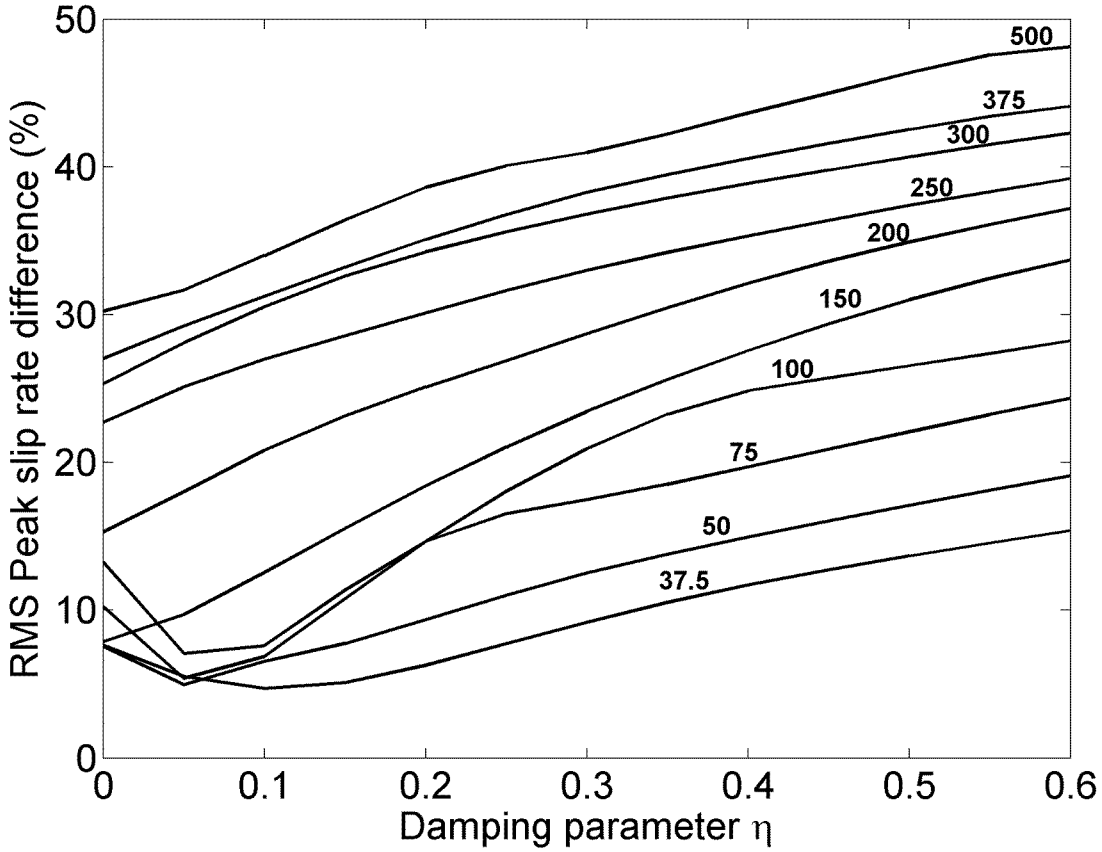

Figure 6(a)

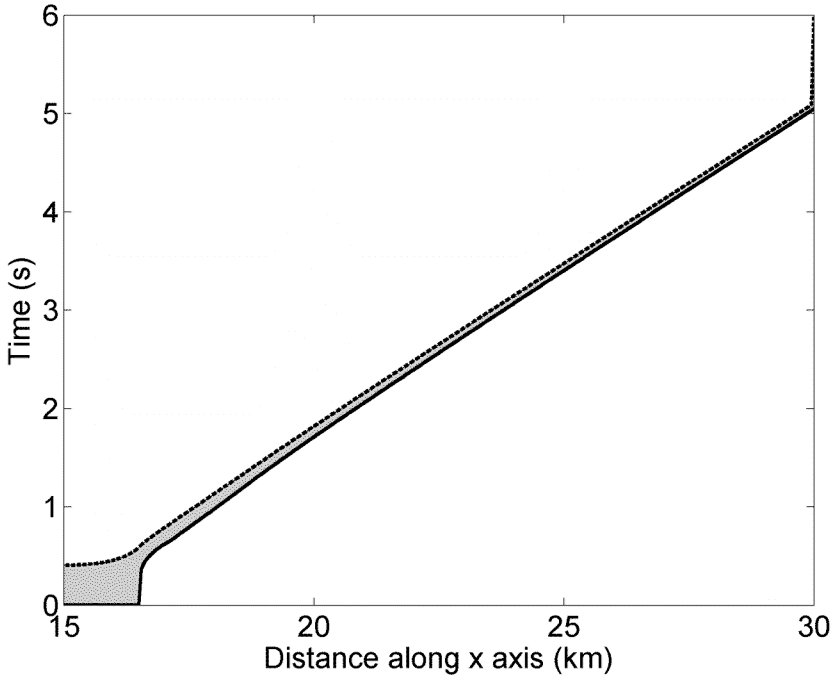

Figure 6(b)

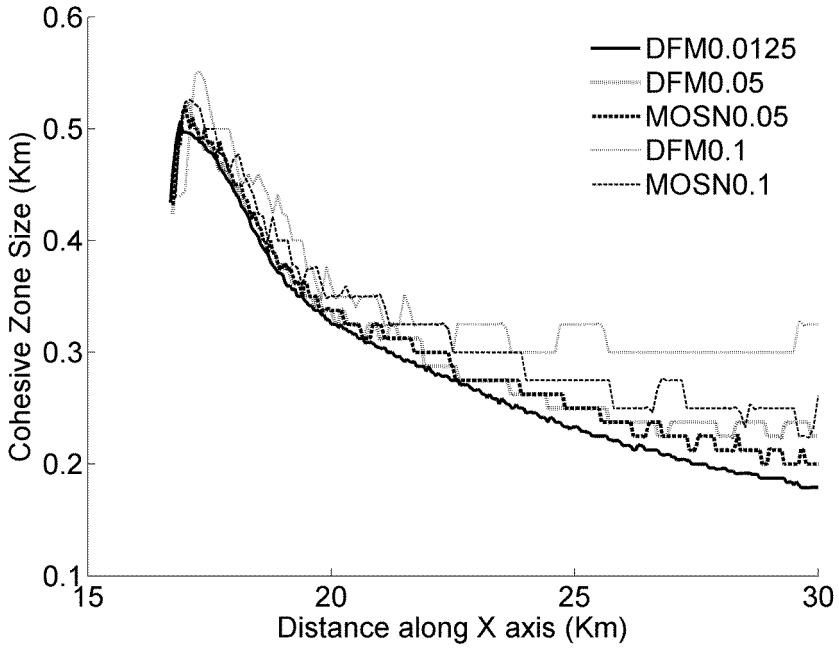

Figure 7

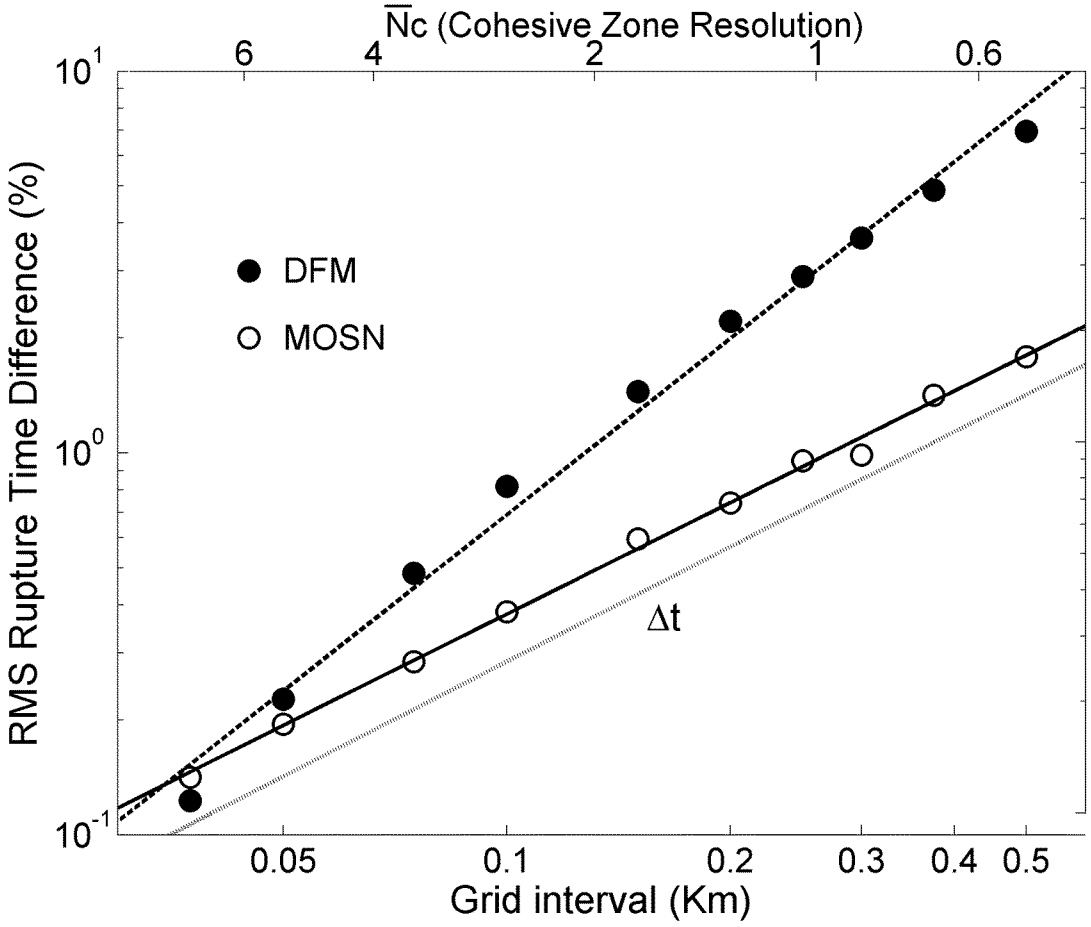
$\overline{Nc}$ (Cohesive Zone Resolution)
6
4
2
1
0.6
10^1
10^0
10^{-1}
RMS Rupture Time Difference (%)
DFM
MOSN
Δt
0.05
0.1
0.2
0.3
0.4
0.5
Grid interval (Km)

Figure 8

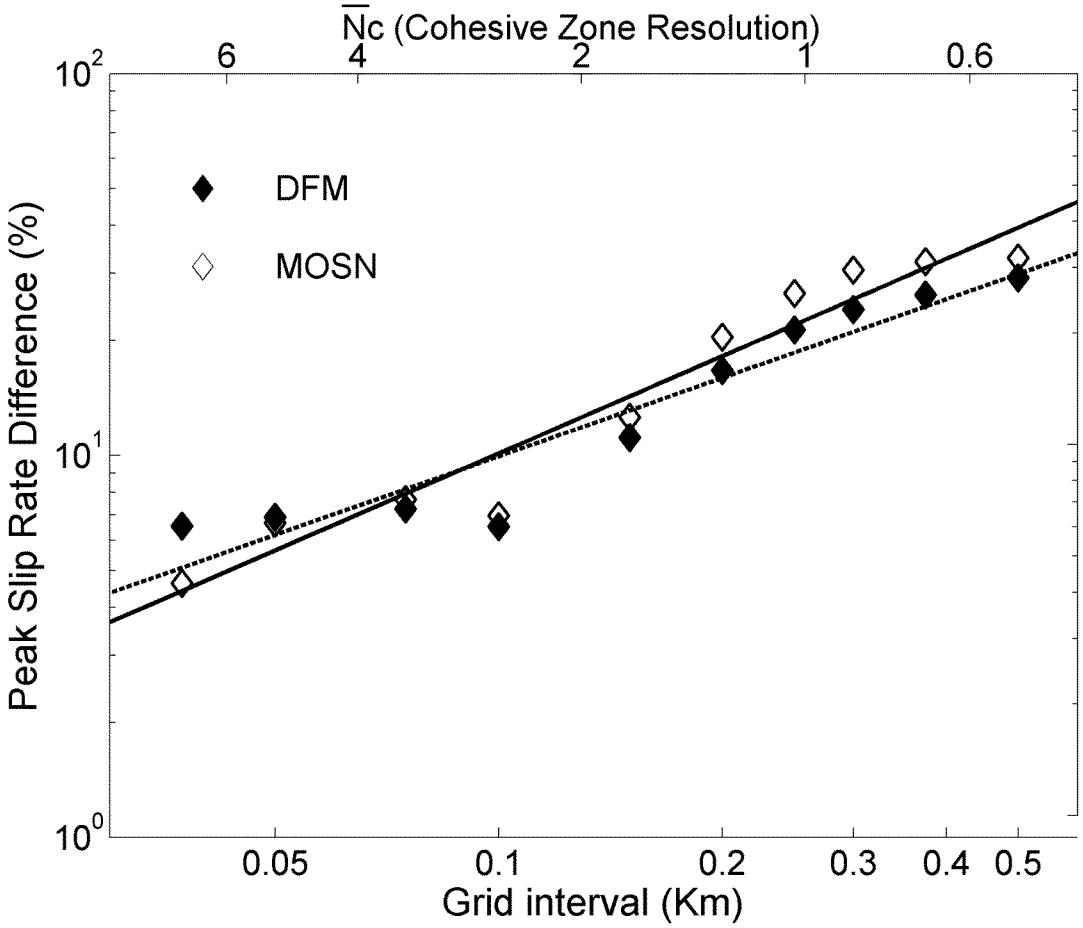
$\overline{Nc}$ (Cohesive Zone Resolution)
6
4
2
1
0.6
10^2
10^1
10^0
DFM
MOSN
Peak Slip Rate Difference (%)
0.05
0.1
0.2
0.3
0.4
0.5
Grid interval (Km)

Figure 9

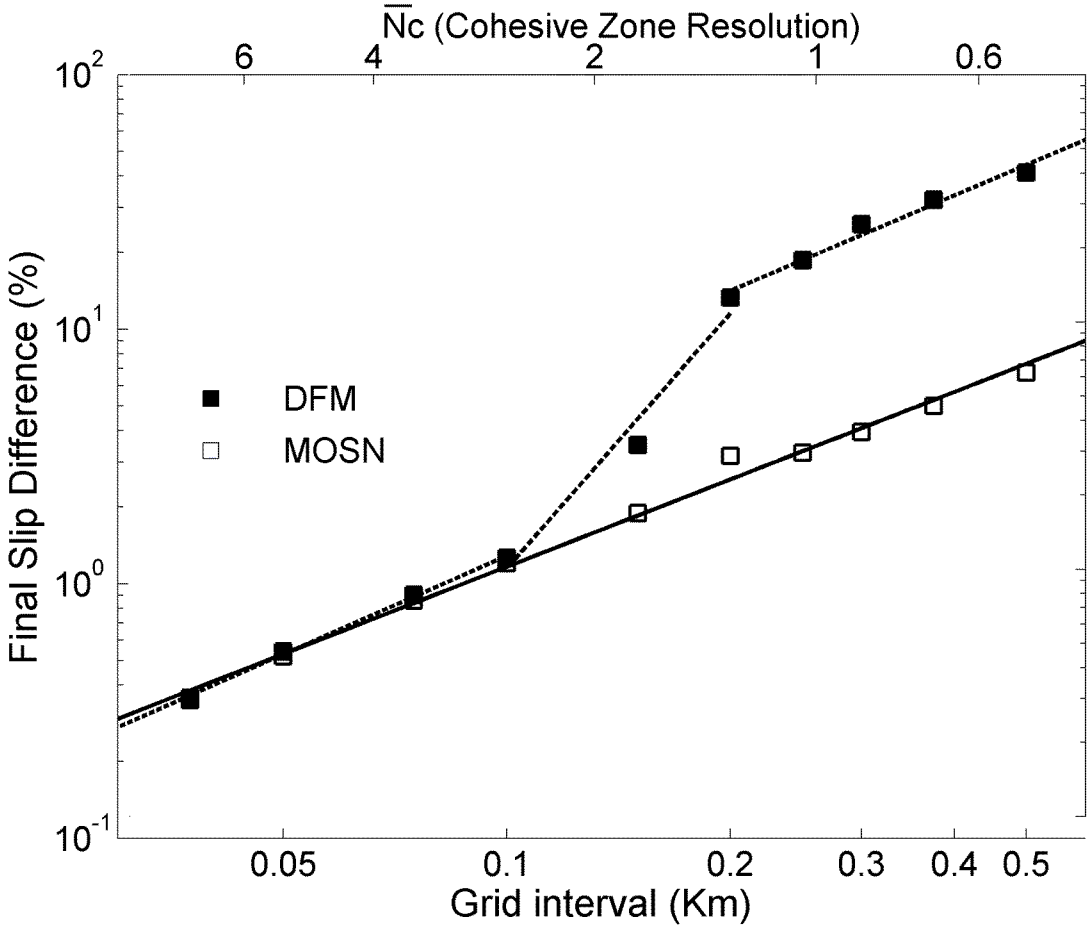
$\overline{Nc}$ (Cohesive Zone Resolution)
6
4
2
1
0.6
10^2
10^1
10^0
10^{-1}
Final Slip Difference (%)
DFM
MOSN
0.05
0.1
0.2
0.3
0.4
0.5
Grid interval (Km)

Figure 10

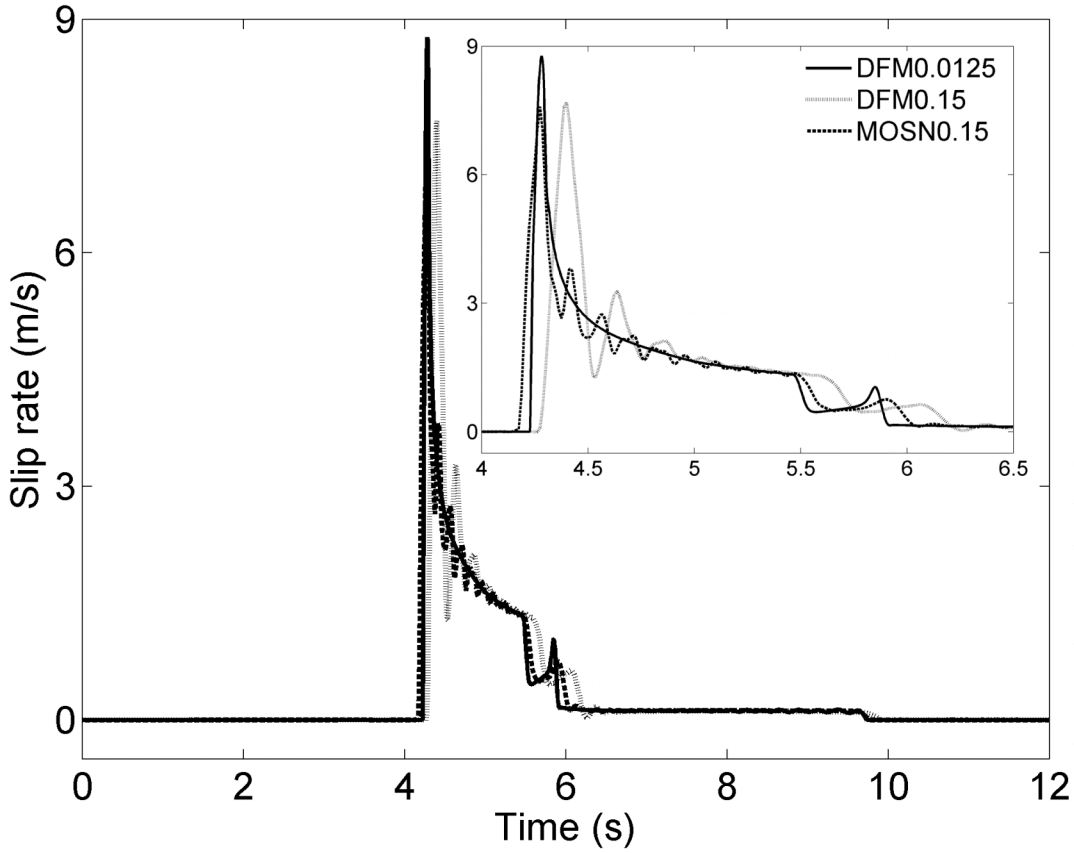

Figure 11

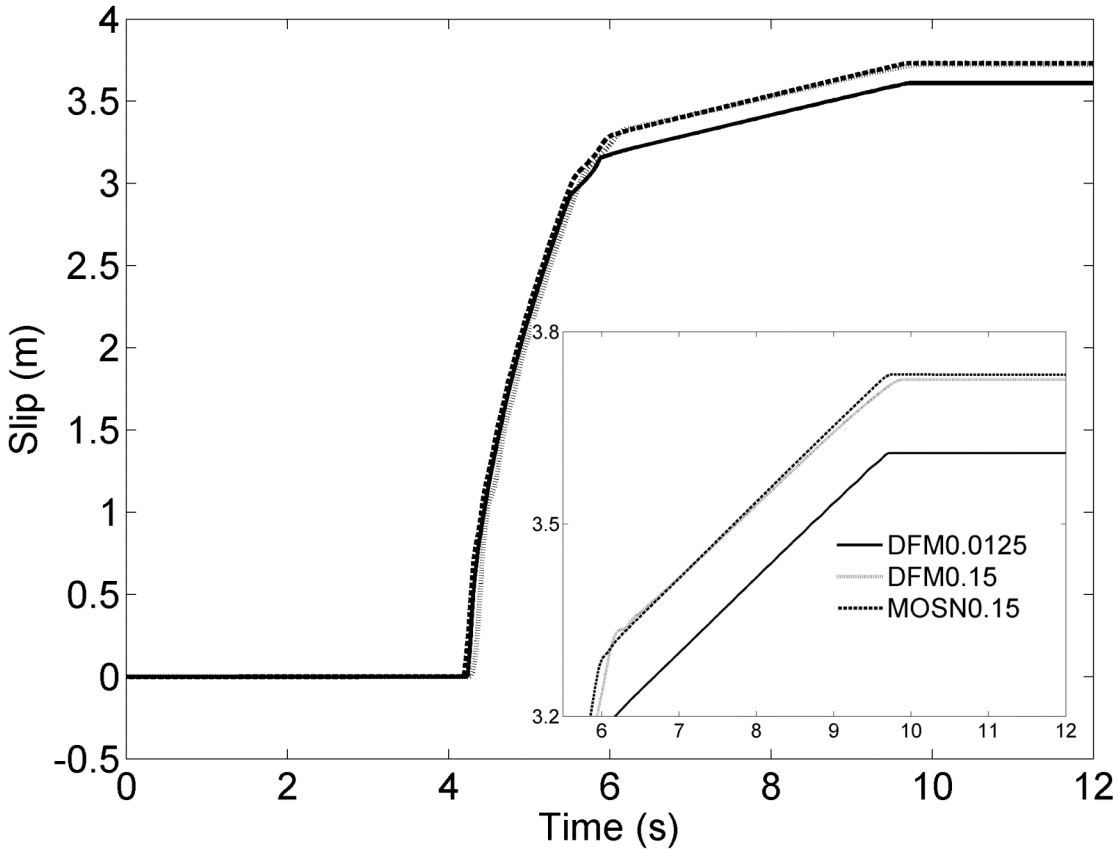

Figure 12